Self-consistent inner magnetosphere simulation driven by a global MHD model

Sorin Zaharia,[1] V. K. Jordanova,[1] D. Welling,[1] and G. Tóth[2]

[1]   We present results from a one-way coupling between the kinetic Ring Current Atmosphere Interactions Model with Self-Consistent B field (RAM-SCB) and the Space Weather Modeling Framework (SWMF). RAM-SCB obtains plasma distribution and magnetic field at model boundaries from the Block Adaptive Tree Solar Wind Roe Upwind Scheme (BATS-R-US) magnetohydrodynamics (MHD) model and convection potentials from the Ridley Ionosphere Model within SWMF. We simulate the large geomagnetic storm of 31 August 2005 (minimum SYM-H of −116 nT). Comparing SWMF output with Los Alamos National Laboratory geostationary satellite data, we find SWMF plasma to be too cold and dense if assumed to consist only of protons; this problem is alleviated if heavier ions are considered. With SWMF inputs, we find that RAM-SCB reproduces well storm time magnetosphere features: ring current morphology, dusk side peak, pitch angle anisotropy, and total energy. The RAM-SCB ring current and *Dst* are stronger than the SWMF ones and reproduce observations much better. The calculated field-aligned currents (FAC) compare reasonably well with 2 h averaged pictures from Iridium satellite data. As the ring current peak rotates duskward in the storm main phase, the region 2 FACs rotate toward noon, a feature also seen in observations. Finally, the RAM-SCB magnetic field outperforms both the dipole and the BATS-R-US field at Cluster and Polar spacecraft locations. This study shows the importance of a kinetic self-consistent approach and the sensitive dependence of the storm time inner magnetosphere on plasma sheet conditions and the cross polar cap potential. The study showcases the RAM-SCB capability as an inner magnetosphere module coupled with a global MHD model.

1.   Introduction

[2]   During geomagnetic storms, the dipole approximation for the magnetospheric magnetic field breaks down even in the inner magnetosphere. This was first discovered more than 40 years ago [*Cahill*, 1966]; based on Explorer 26 magnetometer measurements during the storm of 17–18 April 1965 (peak *Dst* = −160 nT), *Cahill* [1966] found a duskside near-equatorial field depression from dipole field of −217 nT at $R \approx 3.5 R_E$ (i.e., 30% of the dipole field).

[3]   These storm time field depressions appear due to the diamagnetic effect of large plasma pressure, which distorts the field. The modified magnetic field strongly changes the ring current particle paths and evolution. Due to plasma-field interaction, accurate knowledge of the field is deeply tied to knowledge of the plasma structure and dynamics. An accurate description of the magnetic field is also needed for understanding and describing the dynamics of radiation belt particles [*Selesnick and Blake*, 2000].

[4]   One class of models describing the magnetospheric magnetic field are empirical field models [e.g., *Olson and Pfitzer*, 1974; *Tsyganenko and Stern*, 1996], which postulate a framework of electrical currents, with model parameters obtained by fitting the resulting magnetic field to many observations at different locations and times. If trained with storm time data, such models can describe the inner magnetosphere field depressions during storms [e.g., *Tsyganenko et al.*, 2003]. Such models show for example that during a storm with a minimum *Dst* index of −250 nT, the dipole approximation is invalid as close to Earth as 2.5 R_E. While empirical models provide realistic large-scale fields on a statistical, averaged basis, they have a few known shortcomings, among them the following: (1) they represent average states rather than instantaneous magnetospheric configurations (even though they can be modified to better reproduce event-based magnetic fields [e.g., *Ganushkina et al.*, 2002; *Kubyshkina et al.*, 2009]) and (2) they do not have built-in exact force balance between field and plasma pressure, as exact force balance imposes additional constraints [*Zaharia and Cheng*,

[1]Space Science and Applications, Los Alamos National Laboratory, Los Alamos, New Mexico, USA.
[2]Center for Space Environment Modeling, University of Michigan, Ann Arbor, Michigan, USA.

2003] (depending on model and activity level, approximate pressures can still be obtained in a least square sense [*Tsyganenko*, 2010]).

[5] Another class of models are the first principle physics-based numerical models, which compute both fields and plasmas based on the fundamental equations of plasma physics. The most widespread class of such models are the global magnetohydrodynamics (MHD) models [*Lyon et al.*, 1981; *Ogino*, 1986; *Raeder et al.*, 1995; *Janhunen*, 1996; *Gombosi et al.*, 1998]. However, while they are driven by the solar wind and cover virtually the whole magnetosphere, the MHD formalism cannot accurately describe the inner magnetosphere (closer than 10 R_E from Earth) [e.g., *De Zeeuw et al.*, 2004], because it does not include the energy-dependent gradient/curvature drifts and does not have a heat flux [*Heinemann and Wolf*, 2001].

[6] The plasma pressure computed by global MHD models in the inner magnetosphere is an order of magnitude lower than observed (or obtained when coupled with an inner magnetosphere kinetic model [*De Zeeuw et al.*, 2004; *Toffoletto et al.*, 2004; *Buzulukova et al.*, 2010]); no (or only very weak) ring current forms during storms in MHD models. While some argue that coarse numerical grid resolution is partly responsible for the MHD shortcomings in the inner magnetosphere, to our knowledge no published study exists showing that increased resolution in MHD models in the near-Earth region leads to ring current and *Dst* results similar to those obtained by kinetic "drift models" [*Buzulukova et al.*, 2010].

[7] A separate subclass in the physics-based model category, the drift models employ a kinetic approach by solving the (bounce-averaged) Boltzmann equation for the particle distribution function, either with the assumption of isotropy (the RCM model [*Harel et al.*, 1981]) or including full pitch angle anisotropy [*Jordanova et al.*, 1994; *Fok et al.*, 1995]. These models include all relevant particle drifts in the inner magnetosphere; as the drifts are different for different particle energies, the energy discretization of these models is in effect equivalent to a cross-field heat flux [*Heinemann and Wolf*, 2001].

[8] From a theoretical point of view, *Heinemann and Wolf* [2001] clearly proved what the MHD formalism lacks compared to the "drift physics" approach, namely, diamagnetic drift velocity and heat flux. Regarding the former, the MHD formalism assumes the "small Larmor radius" approximation. This approximation assumes that the **E** × **B** drift magnitude is much larger than the magnitude of the gradB/curvature drifts. This is clearly not the case in the inner magnetosphere for ring current (and higher) energy (a few to hundreds of keV) particles. In other words, ideal MHD is appropriate for describing relatively fast fluid motions, in which there is an imbalance between plasma pressure gradients and magnetic stresses. It is less appropriate for describing the slow (compared to the Alfvén speed) convection typical of the inner magnetosphere.

[9] To our knowledge there has been no study of adding the terms prescribed by *Heinemann and Wolf* [2001] to a global three-dimensional magnetospheric MHD code in order to try to reproduce the full kinetic physics. There have been studies analyzing this issue in a more local setting, however; recently, such a study [*Song et al.*, 2008] has shown that as a practical matter such improvements in magnetospheric fluid models could be problematic, as shock waves tend to form in the simulation.

[10] Because MHD codes are less successful at portraying inner magnetosphere physics, an obvious idea is to use them in other regions of the magnetosphere where they better portray the relevant physics, and couple them with the more physically accurate kinetic codes in the inner magnetosphere. This idea has spawned efforts of using MHD codes to treat the "global" magnetosphere in numerical frameworks, and having other models that better describe specific other regions coupled into them; one such effort is the Space Weather Modeling Framework [*Tóth et al.*, 2005]. Both two-way [*De Zeeuw et al.*, 2004] and one-way [*Toffoletto et al.*, 2004; *Buzulukova et al.*, 2010] coupling between global MHD and inner magnetosphere models have been performed. Those couplings, beyond improving the MHD results in the inner magnetosphere, also provide more realistic electric and magnetic fields to the inner magnetosphere models: while they better reproduce inner magnetosphere particle dynamics in given fields, many kinetic models do not compute those fields self-consistently.

[11] Part of the quest for a better physics description of the inner magnetosphere in numerical models, this paper follows a two-pronged approach: (1) we present an improved inner magnetosphere kinetic model, RAM-SCB, in which the three-dimensional magnetic field is self-consistently computed in force balance with the particle populations, and (2) we show first results from a one-way coupling of this model with the global MHD model and the ionospheric solver in the Space Weather Modeling Framework. RAM-SCB represents a significant improvement over our initial iterative approach of coupling RAM with the force balance solver [*Zaharia et al.*, 2006, 2008; *Jordanova et al.*, 2006, 2010]: it employs full coupling every 5 min and has all the terms updated to use the force balanced magnetic field; in addition, the equilibrium approach uses a new Euler potential technique [*Zaharia*, 2008], allowing for a better, seamless coupling of the equilibrium code with the fixed grid RAM model.

[12] Until recently RAM (and RAM-SCB) have used plasma boundary conditions at geosynchronous orbit from Los Alamos National Laboratory (LANL) satellites (from SOPA [*Belian et al.*, 1992] and MPA [*McComas et al.*, 1993] instruments). RAM has used prescribed empirical electric (**E**) fields (e.g., Volland-Stern [*Volland*, 1973; *Stern*, 1975], Weimer 01 [*Weimer*, 2001]), while we prescribed magnetic flux boundaries for the equilibrium code using empirical magnetic field models such as T89 [*Tsyganenko*, 1989]. In this paper we present results from RAM-SCB simulations with plasma and magnetic boundary inputs from a numerical physics-based model, namely, the Block Adaptive Tree Solar Wind Roe Upwind Scheme (BATS-R-US) code [*Powell et al.*, 1999; *De Zeeuw et al.*, 2000] within the Space Weather Modeling Framework (SWMF) [*Tóth et al.*, 2005]; the driving electric field is taken from the Ridley Ionosphere Model (RIM) [*Ridley et al.*, 2001, 2004] also within SWMF. We run SWMF with the Rice Convection Model (RCM) [*Harel et al.*, 1981] included as well (RCM only provides pressure; the electric field is still from RIM), as we find that setup gives more realistic plasma sheet conditions and cross polar cap potential values than BATS-R-US alone.
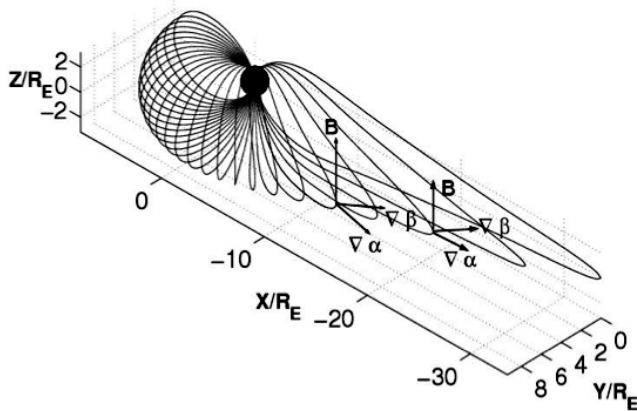
Figure 1. Euler potential representation of the magnetic field ($\mathbf{B} = \nabla\alpha \times \nabla\beta$) in the Earth's magnetosphere.

[13] Our approach in the one-way coupling of RAM-SCB with BATS-R-US is different from just using the MHD magnetic field in the kinetic model, as other studies coupling inner magnetosphere (IM) with MHD models have done. In those studies, the plasma pressure from the IM model is returned to the MHD model gradually and not completely, in order to avoid potential numerical instabilities [*De Zeeuw et al.*, 2004]. In the work presented here, we use the plasma pressure from the kinetic RAM model to obtain the inner magnetosphere magnetic field that is in force balance with the pressure. The main difference between passing the pressure to an MHD code for updating the fields (as done in the past coupling works mentioned above) and our calculation is that our approach allows the inner magnetosphere field to reach full force balance under the ring current pressure gradients. Force balance is expected in the inner magnetosphere, which is a slow flow region [*Wolf*, 1983] most of the time (including during storms, but not substorm expansions). This technique for obtaining the magnetic field ($\mathbf{B}$) is especially important in regions of large plasma β_p (the ratio of plasma to magnetic pressure), because there the pressure critically determines the field; that is, (relatively) small changes in the plasma pressure can lead to very large field changes.

[14] While there is no feedback from RAM-SCB to the MHD code at this stage, this one-way coupling effort paves the way toward a full (two-way) coupling and full inclusion of RAM-SCB within SWMF. The main questions this paper seeks to answer regard the role of self-consistency and kinetic physics in the inner magnetosphere dynamics, and the effect of the plasma boundary (proton plasma versus inclusion of heavy ions) and driving convection electric field; we also seek to find out how well this new model reproduces observed storm time features in the inner magnetosphere, from the ring current peak intensity and location to the development of region 2 field-aligned currents. Two complementary papers focus on distinct, but related, issues of RAM-SCB physics: *Jordanova et al.* [2010] focus on how the self-consistent simulation results compare with those using dipole or empirical magnetic fields (in that work, RAM-SCB driving is done by empirical electric field models and LANL particle data); D. Welling et al. (The effects of dynamic ionospheric outflow on the ring current, submitted to *Journal of Geophysical Research*, 2010) focus on the differences in driving RAM-SCB with different ion compositions: empirically specified O^+ content versus a multispecies MHD approach that includes the Polar Wind Outflow Model [*Glocer et al.*, 2009b].

2. Method: Coupling SWMF ⇒ RAM-SCB

2.1. RAM-SCB: Magnetically Self-Consistent Inner Magnetosphere Model

[15] The RAM-SCB model couples two codes: the ring current atmosphere interactions model (RAM) [*Jordanova et al.*, 1994, 2006] and a 3-D plasma equilibrium code [*Zaharia et al.*, 2004; *Zaharia*, 2008].

[16] On one side of the coupling, RAM solves the bounce-averaged Boltzmann equation for different species (ions and electrons). It uses prescribed convective/corotation electric fields (until recently taken from empirical models), and has been updated to a general $\mathbf{B}$ field geometry [*Jordanova et al.*, 2006, 2010]. The RAM code solves its equations in the plane of minimum B, which is assumed to be the Solar Magnetic (SM) equatorial plane in this work (this approximation essentially neglects magnetotail flaring, which is not as important out to geosynchronous orbit, the present location of the outer model boundary).

[17] On the other side of the coupling in RAM-SCB, the 3-D equilibrium code takes the RAM pressures (in the equatorial plane) and computes a magnetic field configuration in force balance with them by solving the equation $\mathbf{J} \times \mathbf{B} = \nabla \cdot \mathbf{P}$ ($\mathbf{J}$ is the electric current density; the pressure tensor $\mathbf{P}$ is assumed gyrotropic, with the 3 diagonal components $P_\perp$, $P_\perp$ and $P_\parallel$; $\perp$ and $\parallel$ refer to the direction of the magnetic field). The equilibrium code uses an Euler potential representation of the magnetic field [*Cheng*, 1995; *Zaharia et al.*, 2004] (see Figure 1) that has been significantly improved through a generalization that brings great freedom in choosing the Euler potentials and thus the shape and extent of the computational domain [*Zaharia*, 2008]. This allows a complete overlap of the equatorial cross section of the computational domain with the RAM spatial domain (see Figure 2). As magnetic boundary conditions we have used empirical magnetic field models so far [e.g., *Tsyganenko*, 1989; *Tsyganenko and Stern*, 1996]. The equilibrium code computes bounce-averaged quantities for RAM (involving integrals along the magnetic field lines). The geodipole tilt is taken into account by a rotation around the y axis, from the Geocentric Solar Magnetospheric (GSM) to the Solar Magnetic (SM) coordinate system. The magnetic field computed by the equilibrium code at each coupling time step is transferred to RAM to guide the particle evolution. Besides using the new Euler potential formalism, the current version of RAM-SCB also extends our initial, iterative work [*Zaharia et al.*, 2006, 2008; *Jordanova et al.*, 2006] to a full coupling of the 2 codes (a 5 min coupling frequency is used in this study).

[18] For more details on the constituent models of RAM-SCB and their coupling we refer the reader to our previous publications [*Jordanova et al.*, 1996, 2006, 2010; *Zaharia et al.*, 2004, 2006, 2008].
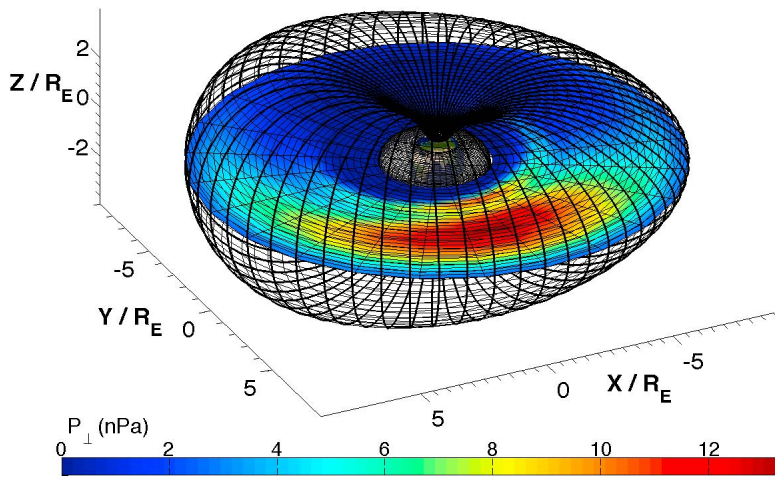
Figure 2. RAM-SCB: coupling of RAM with the 3-D plasma equilibrium code. The thick black lines are magnetic field lines on the outer α Euler potential surface. RAM pressure is shown on the equatorial plane.

2.2. SWMF Inputs for RAM-SCB

[19] Figure 3 is a schematic of RAM-SCB within the Space Weather Modeling Framework (SWMF). Arrows show quantities passed between various components in the framework and the direction of the coupling (red arrows refer to couplings already in effect; blue arrows indicate couplings to be performed in the future).

[20] In this study we explore the one-way coupling SWMF → RAM-SCB, whereby all physical inputs/boundaries in RAM-SCB are obtained from the SWMF simulation. Spe-

cifically, the RAM plasma boundary is prescribed by the BATS-R-US MHD model, which also outputs magnetic field, used for the 3-D equilibrium code boundary within RAM-SCB. RAM is driven with potential electric field calculated by the Ridley Ionosphere Model (RIM) within SWMF. Optionally, SWMF is also run with the RCM component included, as it is found this makes the geosynchronous plasma conditions and the cross polar cap potential drop more realistic. The RAM-SCB model has its outer boundary at geosynchronous orbit in this study.
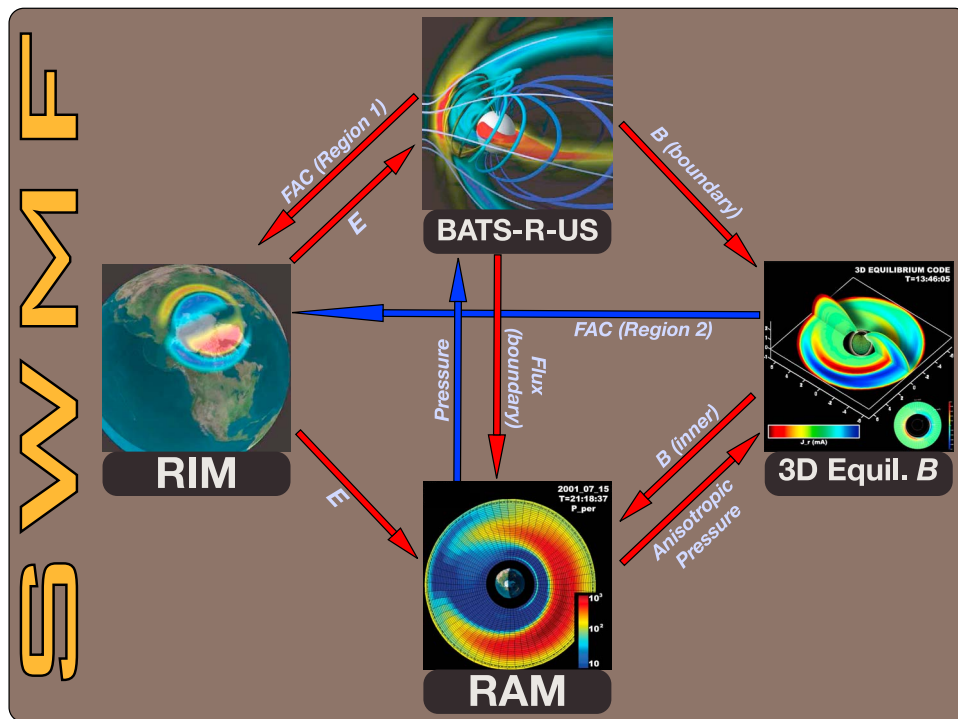

Figure 3. Coupling RAM-SCB inside SWMF. The arrows show the physical quantities that are being passed between various components and the direction of the coupling. Red arrows show existing couplings, and blue arrows show couplings to be achieved in the future.

2.2.1. Space Weather Modeling Framework

[21] The Space Weather Modeling Framework (SWMF) is a framework for space physics applications [*Tóth et al.*, 2005], which integrates separate but interoperating models of physics domains, ranging from the Sun surface to the upper atmosphere of the Earth. The individual models, or "components," run concurrently and exchange information simulating the interaction between the different regions.

[22] The Global Magnetosphere (GM) component in SWMF includes the bow shock, magnetopause, and magnetotail of the planet. The physics of this domain is approximated by the single-fluid MHD equations, and the Block Adaptive Tree Solar Wind Roe Upwind Scheme (BATS-R-US) MHD code [*Powell et al.*, 1999; *De Zeeuw et al.*, 2000] is used. BATS-R-US is an advanced numerical code that uses solution adaptive grids (important in the Earth's magnetosphere, where length scales of interest range across many orders of magnitude). BATS-R-US is scalable for runs on massively parallel computers. The inner boundary of GM is at some distance (2.5 R_E in this work) from the center of the planet, and the inner boundary conditions are given by the Ionosphere Electrodynamics (IE) component (see below). The GM upstream boundary conditions are obtained from the Inner Heliosphere (IH) component or from spacecraft observations.

[23] The ionospheric electrodynamics (IE) component is the Ridley Ionosphere Model (RIM) [*Ridley et al.*, 2004]; it receives field-aligned currents from GM (mapped from the 2.5 R_E MHD inner boundary to the ionosphere) and obtains electric potentials on the ionosphere by solving the Poisson equation with an integrated ionospheric conductivity profile. The conductivity model includes dependence on both field-aligned currents and solar activity EUV. The IE-derived electric potentials are mapped back along the field to GM, creating an ionospheric feedback system.

[24] For the inner magnetosphere (IM), the Rice Convection Model (RCM) [*Harel et al.*, 1981], a kinetic drift model, is currently included [*De Zeeuw et al.*, 2004] in SWMF. In runs with RCM, the BATS-R-US pressures in the inner magnetosphere on closed field lines are modified through gradual nudging toward the RCM values (without quite reaching those values), but are never forced into instantaneous agreement to avoid potential numerical instabilities [*De Zeeuw et al.*, 2004]. Therefore, the MHD pressure gradients are never as large as in RCM. Also, in the fully dynamic MHD code, the modified pressure gradients likely lead to both field stretching and inertial effects, according to the full MHD momentum equation. In RAM-SCB, on the other hand, we compute magnetic fields in full force balance with plasma pressure gradients, as inertial effects are neglected in the "slow flow" approximation ($V \ll V_A$, the Alfvén speed) in the inner magnetosphere.

[25] While SWMF is capable of simulating a huge domain spanning from the Sun surface to the Earth's upper atmosphere, it can also be run in a more limited mode with fewer models. Here we run it with 2 or 3 components, described above: the global magnetosphere (GM) and the ionosphere electrodynamics (IE), with optionally the RCM inner magnetosphere component included as well. The rationale for adding RCM is that the present study takes boundary values at geosynchronous orbit, where MHD and MHD+RCM outputs can be very different: storm time RCM values for thermal energy density (pressure) can exceed MHD values by an order of magnitude or more near geosynchronous orbit [*Toffoletto et al.*, 2004; *De Zeeuw et al.*, 2004].

[26] In the present simulation setup, the BATS-R-US simulation is driven by actual time-shifted upstream solar wind measurements from the ACE spacecraft at the L1 Lagrangian point.

2.2.2. Plasma Boundary

[27] Plasma pressure is taken from SWMF output at geosynchronous orbit in this study. A Maxwellian distribution function is assumed, with the MHD fluid quantities being moments of this distribution. With this assumption, we prescribe isotropic differential particle flux on the RAM boundary as

$$J_d = \frac{2E}{m^2} f(E) = \frac{2nE}{\sqrt{m}(2\pi T)^{3/2}} \exp\left(-\frac{E}{T}\right) \tag{1}$$

[28] The flux is only isotropic on the boundary (because the MHD pressure is isotropic). The different dynamics for particles with different pitch angles in the kinetic RAM code leads to development of pitch angle anisotropy at all other locations inside the RAM-SCB domain.

[29] If the plasma contains more than one ion species (i.e., it includes heavy ions like O^+), the MHD mass density on the IM boundary will correspond to a lower particle density than if all particles were protons (H^+). If we assume that O^+ and He^+ ions are present besides H^+ and we denote $n_{O^+}/n_{H^+} = \mathcal{B}$ and $n_{He^+}/n_{H^+} = \mathcal{G}$, we have

$$[n] = n_{H^+}[1 + 4\mathcal{G} + 16\mathcal{B}] \tag{2}$$

where $[n]$ is the particle density obtained from the MHD output, assuming all ions are protons. For the same mass density, one thus obtains significantly lower particle density if heavier ions in the plasma are considered as well; such ions (e.g., O^+) are a significant proportion (>15% of the total number density) of the magnetospheric ions during geomagnetic storms [e.g., *Gloeckler and Hamilton*, 1987].

[30] In this study we include both O^+ and He^+ ions in addition to protons, and we ascribe ion composition ratios using the empirical formula obtained by *Young et al.* [1982] by analyzing 48 months of data taken by the Ion Composition Experiments on the ESA/GEOS 1 and 2 satellites at or near geostationary orbit:

$$n_{O^+}/n_{H^+} = 4.5 \times 10^{-2} \exp\left[0.17K_p + 0.01F_{10.7}\right] \tag{3}$$

[31] The *Young et al.* [1982] formula depends on magnetospheric activity (through Kp) and solar EUV flux (through $F_{10.7}$). While no storm time dependence is explicitly included, this formula leads to an O^+ content increase by about a factor of 8 during significant geomagnetic activity versus quiet times. The *Young et al.* [1982] study also provides the He^+/H^+ ratio; however, this is small at all times (~5 %) and does not depend on activity. Nevertheless, we do include He^+ as one of the ion species in the RAM code.

[32] Besides mass density, another quantity provided by the MHD code on the RAM-SCB boundary is plasma

pressure (P). With a lower particle density (if heavy ions are included), plasma temperature must be increased proportionally to keep the pressure (thermal energy density) the same. The lower density and higher temperature in the presence of heavy ions (versus a proton plasma alone) might alleviate the "cold and dense" plasma sheet output sometimes encountered in global MHD simulations [*Jichun Zhang et al.*, 2007].

[33] We remark that keeping the same particle density (calculated from MHD assuming only H^+) is not at first sight a reasonable alternative if the plasma also contains other ion species, since doing so would not conserve mass density. However, in the SWMF runs in this study no ionospheric source is prescribed, from which one could argue that the total particle density (and in particular O^+) is lower if taking mass density and using equation (2) than if additional ionospheric outflow were considered. An explicit choice for obtaining O^+ outflow is using the polar wind outflow module inside the SWMF, PWOM [*Glocer et al.*, 2009b]. A comparison of single-fluid (no PWOM) versus multifluid (with PWOM) SWMF output is presented by Welling et al. (submitted manuscript, 2010).

2.2.3. Magnetic Field Boundary

[34] The most challenging part of the SWMF → RAM-SCB coupling involves matching the magnetic fields: unlike in the case of the pressure (coupled in the SM equatorial plane), the magnetic coupling is three-dimensional.

[35] The 3-D force balance code requires inner and outer Euler potential α surfaces defining its computational domain, and also the value of α on those surfaces. In the past we constructed the domain for inner magnetosphere simulations by field line tracing using the T89 empirical model [*Tsyganenko*, 1989]. Here we use the BATS-R-US magnetic field and compute a different domain at each coupling time step (5 min cadence). We trace the BATS-R-US field lines using parallel tracing routines in SWMF [*De Zeeuw et al.*, 2004; *Glocer et al.*, 2009a] and construct a magnetic shell (of constant α), consisting of field lines with equatorial foot points along the RAM-SCB domain perimeter. The tracing is extended in the gap region from the SWMF inner sphere of radius 2.5 R_E to the Earth's surface, by assuming a dipole field there.

[36] The magnetic domain cross section (intersection of the equatorial plane with the outer α surface) is chosen to be a circle of radius 6.75 R_E (this fully envelops the RAM domain that extends to 6.5 R_E and also includes its boundary "ghost cells" at $R = 6.75$ R_E). Such an exact specification for the equatorial plane cross section of the domain is possible with our new Euler potential method [*Zaharia*, 2008]. Using the SWMF tracing, we obtain the latitudes of the field lines that have their equatorial foot points on this circle. The difference between the magnetic flux for the different latitudes and that for a latitude of reference is a function $F(\beta)$, which is used in constructing the equilibrium code domain. The procedure for obtaining $F(\beta)$ is described by *Zaharia* [2008]. We use a dipole field to obtain α surfaces in the $L = 2$ to $L = 2.5$ R_E region (the BATS-R-US domain only starts from 2.5 R_E). For both the inner α boundary and all α surfaces inside the computational domain we perform field tracing from the latitudes obtained using $F(\beta)$, as described by *Zaharia* [2008]. This provides us with both inner and outer α boundaries and also represents an initial guess for the magnetic field inside the RAM-SCB domain.

2.2.4. Electric Field Input

[37] Previously RAM has used primarily empirical convection electric fields (e.g., the Volland-Stern (V/S) [*Volland*, 1973; *Stern*, 1975] or the Weimer models [*Weimer*, 1996, 2001]). In this study we use the output from the RIM model [*Ridley et al.*, 2001] within SWMF; the RIM convection potentials are mapped along the self-consistent magnetic field lines (under the assumption that the field line is equipotential) to obtain the equatorial convection electric field that drives RAM. Note that the simulations presented here do not include the electric field induced by the time change of the magnetic field. An initial calculation of the induced electric fields from time sequences of self-consistently computed magnetic fields was performed by *Zaharia et al.* [2008]. The full inclusion of the induced electric fields in the RAM-SCB code is a work in progress, and will be reported in a future publication.

2.2.5. Computational Details of the Simulations

[38] We run both a two-component (BATS-R-US+RIM) and a three-component (BATS-R-US+RCM+RIM) SWMF. The BATS-R-US grid is limited by $X = [-224, 32]$ R_E, $Y = [-128, 128]$ R_E and $Z = [-128, 128]$ R_E (the total number of computational cells is ~1.8×10^6; the grid resolution in the near-Earth region is 1/4 R_E (in a rectangular box -16 R_E < X < 8 R_E, -8 R_E < Y < 8 R_E, -4 R_E < Z < 4 R_E). The resolution is further refined to 1/8 R_E inside a sphere of radius 5.25 R_E (mainly for accurately calculating the field-aligned currents in BATS-R-US). We chose the Rusanov second-order numerical scheme with the minmod slope limiter [*Roe*, 1986]. As mentioned, the BATS-R-US inner boundary is taken to be a sphere of radius $R = 2.5$ R_E (going down to 1 R_E is not computationally feasible, as the high magnetosonic speed in the regions of large magnetic field close to Earth places too low a bound on the maximum time step in the Courant-Friedrichs-Lewy (CFL) condition [*Courant et al.*, 1967]).

[39] The RAM-SCB code undergoes coupling of the 2 constituent models every 5 min. The resolution in the 3-D equilibrium code is 51 × 35 × 61 grid points, while the RAM spatial resolution is 20 × 25 points in the equatorial plane (in addition to the spatial grid, RAM also has 36 × 72 points in the energy–pitch angle space). The chosen grid resolution is a good compromise between speed and numerical accuracy: comparisons with results with higher number of grid points (e.g., 49 azimuthal grid points in RAM instead of 25) did not show significant differences that would indicate strong numerical diffusion. We use a monotonized central (MC) slope limiter [*Van Leer*, 1977] in RAM with $r = 1.2$, which improves numerical stability compared to the previously used superbee limiter [*Roe*, 1986]. The RAM-SCB code runs 1.5× faster than real time with the above grid resolution on a 2.66 GHz Apple desktop machine. We note that the present resolution for the equilibrium code is coarser than the one we used in other applications, such as obtaining background states for ballooning instability studies [*Cheng and Zaharia*, 2004]. With the coarser resolution, the quality of the equilibrium obtained is also impacted: in this work we stop the Picard iteration process (in the equilibrium code) once the changes in α and β from one iteration to the next are less than 5%. Higher-quality equilibria can be obtained with more computational grid points, in which the global force imbalance, defined as $\|\mathbf{J} \times \mathbf{B} - \nabla \cdot P\|$,
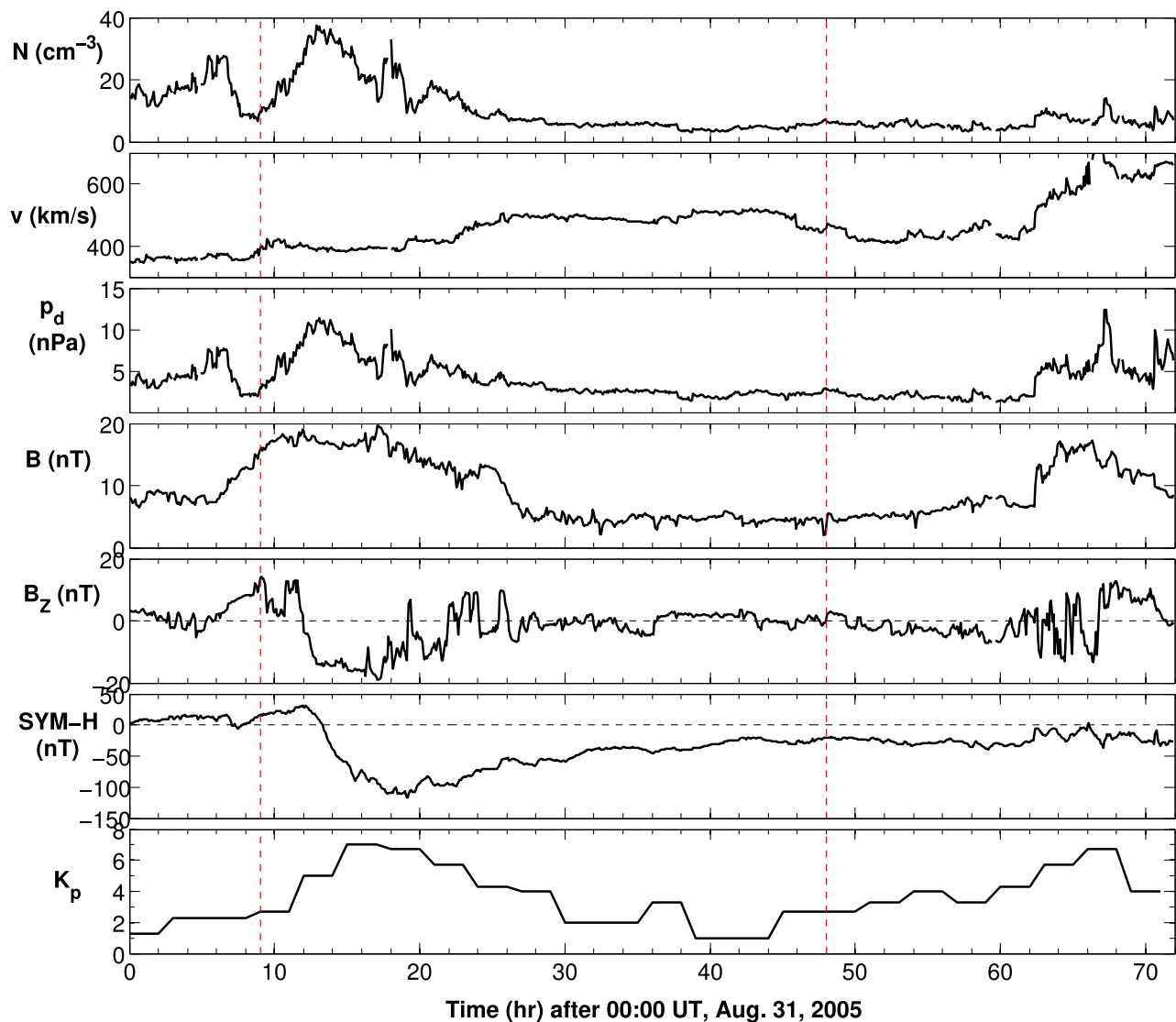
Figure 4. Solar wind parameters, SYM-H, and *Kp* for the simulated storm. Data are taken from the OMNI database; the 40 h interval simulated is delimited by the two vertical red lines.

decreases by a factor of up to 100 [*Zaharia et al.*, 2004]). Such equilibria are needed for studies such as ballooning instability; however, they come with a heavy computational price. The coarse resolution/less exact equilibria used here are sufficient, however, for the present purpose, namely, to quantify the effect of the depressed field on the particle drifts. This effect is quantified through the integrals $h = 1/(2R_0)\int ds/ \sqrt{1 - B(s)/B_m}$ and $I = 1/R_0 \int \sqrt{1 - B(s)/B_m}ds$, which are functions of the magnetic field geometry [*Jordanova et al.*, 2006; *Zaharia et al.*, 2006]. We have investigated the effect of increasing the number of grid points in the equilibrium code and have found that such resolution increase, while allowing a larger decrease of the global force imbalance, does not change the magnetic field geometry (or the integrals *h* and *I*) much compared to computations with the coarser grid used in this study.

[40] We note that plasma macroinstabilities (mirror, firehose) are not considered in our approach. Because it lacks an MHD-like equation of state (the pressure is externally

given), the equilibrium code can, however, compute unstable states (e.g., ballooning [*Cheng and Zaharia*, 2004]), so numerically this is not a problem. Also, for the case $P_\perp > P_\parallel$ the anisotropy can be decreased by particle interaction with ion cyclotron waves as well (however, in preliminary anisotropic MHD studies [*Meng et al.*, 2009] we found that the $P_\perp/P_\parallel$ threshold for the mirror instability can sometimes be lower than that of the ion cyclotron mode).

2.3. The 31 August 2005 Geomagnetic Storm

[41] The geomagnetic storm simulated in this study occurred during 31 August to 2 September 2005 and has been selected for study by the NASA Living With a Star Focus Team on "Effects of Ionospheric-Magnetospheric Plasma Redistribution on Storms." It is a large storm (minimum SYM-H = −116 nT, maximum *Kp* = 7), caused by a corotating interaction region (CIR) [*Jie Zhang et al.*, 2007].

[42] To obtain the RAM-SCB model inputs, we first run the Space Weather Modeling Framework simulation, driven

by the observed upstream solar wind parameters (time-shifted to the sunward edge of the domain at $X = 32\ R_E$), for 40 h starting at 0900 universal time (UT) on 31 August 2005. This time interval is shown within red vertical lines in Figure 4, which displays, from top to bottom: solar wind density (N), solar wind speed (V), solar wind dynamic pressure p_d, total magnitude of the interplanetary magnetic field (IMF) (B), north-south component of the IMF (B_z, in GSM coordinates), as well as SYM-H and Kp indices. All the data are from the NASA OMNI database: solar wind data and SYM-H are displayed with a 5 min resolution, while K_p is interpolated every hour (we consider SYM-H (1 min resolution) rather than the Dst index (1 h resolution) as its much higher time resolution will allow us a better comparison with computed output, available every 5 min (the frequency of the model coupling); as SYM-H is a de facto high-resolution of Dst [*Wanliss and Showalter*, 2006], for the computed results, we also use "SYM-H" and "Dst" interchangeably in the text).

[43] The 31 August 2005 event solar wind conditions are characterized by a region of increased density (particle density starts to increase at 0900 UT and reaches a maximum value of 36 cm^{-3} at ~1400 UT) and southward IMF (the IMF turns southward at ~1200 UT, reaching a largest negative value of −19 nT at ~1700 UT; it then begins a gradual northward rotation). These solar wind conditions led to the geomagnetic storm, with minimum SYM-H = −116 nT at hour 19. The Kp index reached a maximum value of 7, from hours 15 to 18. The storm recovery lasted several days.

[44] The simulated 40 h interval starts at 0900 UT on 31 August 2005, before the beginning of the storm and covers the whole main phase as well as a significant part of the recovery phase. The start of the simulation coincides with the increase in the solar wind ram pressure.

[45] For this initial study we use a centered dipole for the Earth's internal magnetic field (both in RAM-SCB and SWMF). While the RAM-SCB computations are performed in the SM equatorial plane, the RAM-SCB output is transformed to GSM to take into account the geodipole tilt and allow a realistic comparison with in situ satellite observations.

3. Simulation Results

3.1. SWMF Output: Comparison With Observed Geosynchronous Particle Fluxes

[46] We compare (Figure 5) particle fluxes corresponding to the Maxwellian distribution obtained from SWMF (BATS-R-US+RCM) density (n) and temperature ($T = P/n$) with particle data from LANL geosynchronous satellite MPA [*McComas et al.*, 1993] and SOPA [*Belian et al.*, 1992] instruments, energy range from 88 eV to 900 keV. Figure 5 shows the fluxes at 3 magnetic local times (2100 MLT, 0000 MLT and 0300 MLT) and 3 times during the storm (hour 12, before the storm; hour 19, at the storm peak; and hour 36, in the recovery phase). The LANL data is averaged over 5 min, and at each local time it is interpolated among the data from all available LANL satellites on the night side.

[47] The computed flux values at storm peak (hour 19) and in the recovery phase (hour 36) are largest in the premidnight region (2100 MLT (Figure 5, bottom)), consistent with a plasma pressure peak in the dusk sector in the BATS-

R-US+RCM simulation. The same relationship is not as clear, however, in the observed values; in particular, LANL data displays a flux peak at lower energy (~2 keV) in the postmidnight sector (0300 MLT), possible due to an injection not captured by the SWMF.

[48] With the assumption of H^+ being the only ion species, we find (dashed lines in Figure 5) higher computed flux values and at lower energies than observed; this reflects a too cold, too dense plasma sheet in the SWMF simulation if the MHD fluid is assumed to consist of protons only; a too-cold, too-dense plasma sheet was also found in other global MHD simulations [e.g., *Jichun Zhang et al.*, 2007]. The computed flux values with only H^+ are especially large (more than an order of magnitude larger than LANL fluxes) at the beginning of the storm (hour 10, dashed green curves in Figure 5). This cold, dense plasma on the RAM-SCB boundary will be injected deep into the inner magnetosphere and lead to an unrealistic ring current, much stronger than observed, as discussed in section 3.3.

[49] However, if O^+ is taken into account (with the ion composition given by the *Young et al.* [1982] formula), both the computed flux values and their energy range reproduce much better observed values at geosynchronous orbit (solid lines in Figure 5). There is still a discrepancy in the flux functional shape at low energies ($E < 1$ keV), which shows that the actual particle distribution is not Maxwellian; nevertheless, particles at those energies do not contribute significantly to the ring current pressure. The fluxes of a few keV ions also tend to be underestimated (at 0300 and 0000 MLT), however, only after the main phase (at hours 19 and 36, but not hour 10); this mitigates the effect this underestimate might have on the ring current injection.

[50] To further illustrate the change in total particle density and temperature considering O^+ and He^+, in Figure 6 we plot the ratio $r = [n]/(n_{H^+} + n_{O^+} + n_{He^+}) = T_{H^+only}/T_{allions}$ as a function of time for the simulated event. It is remarkable that even before the storm, taking into account O^+ and He^+ leads to a 3 times more tenuous (and hotter) plasma at geosynchronous orbit. At the peak of the storm, the ratio is 5.

3.2. SWMF Output: Electric Potential Patterns

[51] The Cross Polar Cap Potential drop (CPCP) obtained from the SWMF simulation is shown in Figure 7. It is an average of the northern and southern hemisphere values. The maximum CPCP value for the BATS-R-US run only (blue line) is 230 kV, occurring at ~1800 UT. With RCM included, the magnitude of the CPCP (red line) is lower throughout the simulated interval: the maximum value in that case is 199 kV, also occurring at ~1800 UT.

[52] Also shown (black line) in Figure 7 is the CPCP derived by the Assimilative Mapping of Ionospheric Electrodynamics (AMIE) [*Richmond and Kamide*, 1988]. Throughout the storm main phase (hours 12 to 18), the AMIE CPCP (average value 125 kV) is lower than both SWMF-obtained values, but closer to the BATS-R-US+RCM case (~160 kV) than the results with BATS-R-US alone (~210 kV). This shows that the addition of RCM into the SWMF leads to a more realistic cross-polar cap potential drop, a crucial quantity in driving inner magnetosphere dynamics.

[53] The electric potentials (from the SWMF run with RCM) mapped onto the equatorial plane (along RAM-SCB
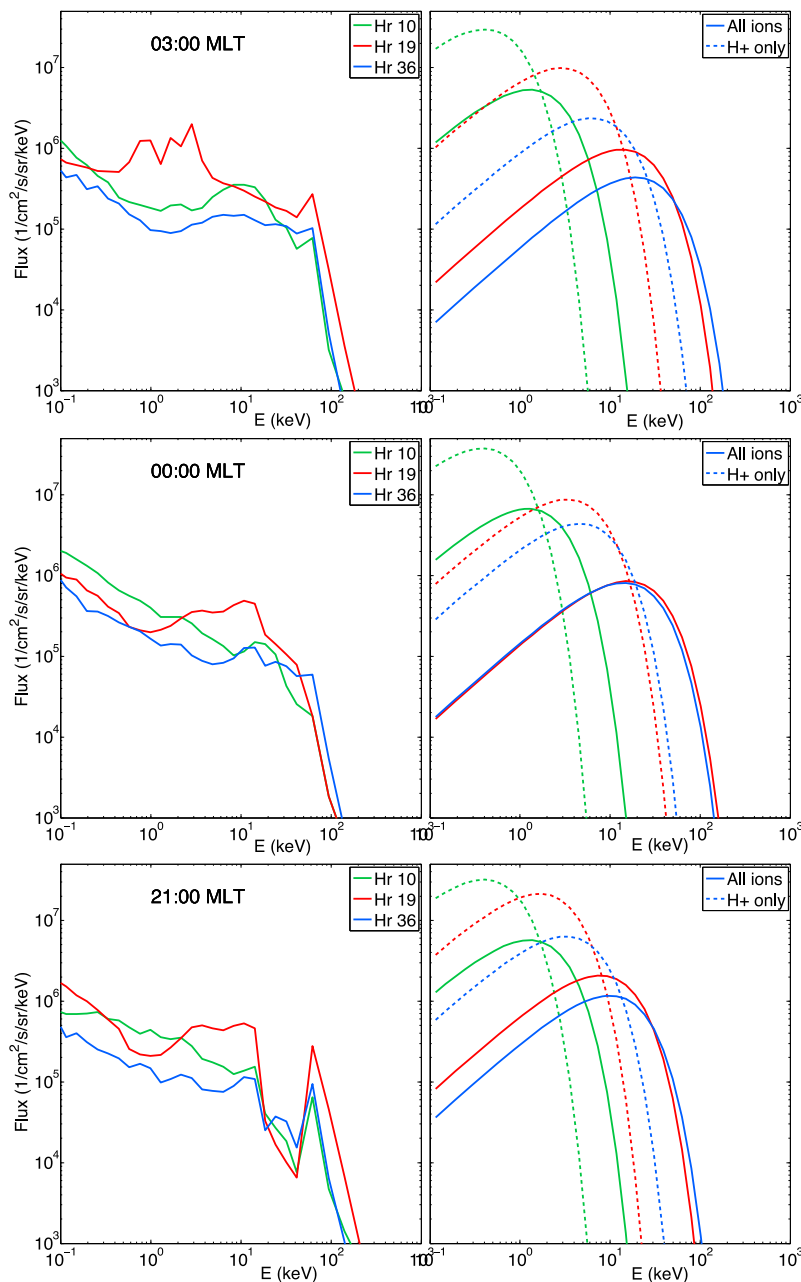
Figure 5. (left) Observed (LANL MPA+SOPA) and (right) SWMF-derived (BATS-R-US+RCM) geosynchronous differential particle fluxes at three different times during the event (hours 10, 19, and 36) and at three local times (0300 MLT, 0000 MLT, and 2100 MLT). The LANL data are interpolated in local time among the available satellites.

magnetic field) are presented in Figure 8 (left), at 5 representative times throughout the storm: T_1 = 10 h (before the southward turning of IMF **B**), T_2 = 15 h (in the main phase, time of large southward IMF B_z), T_3 = 19 h (minimum SYM-H), T_4 = 21 h (early recovery phase) and T_5 = 36 h (recovery). Also shown in Figure 8 (right) is the empirical Volland-Stern (V/S) pattern (nonskewed, i.e., east-west symmetric). The SWMF potential map shows stronger electric field, both in the main and the recovery phase, than that predicted by the Kp-dependent V/S model. At T_2 = 15 h, the RIM potential drop in the domain is largest at ~125 kV, compared with 100 kV predicted by the V/S model. The RIM potential

pattern is also asymmetric: the negative cell has a −85 kV minimum potential, compared to 40 kV maximum in the positive cell. The pattern is also significantly skewed in the post-midnight sector.

3.3. Ring Current Plasma Pressure and *Dst*

[54] The RAM-SCB code is run for the 40 h duration described, with fluxes obtained from the BATS-R-US+RCM simulation, and electric potentials from the RIM model, mapped along the self-consistent magnetic field lines to the equatorial plane. As the initial condition for the RAM particle distribution (H^+, O^+, and He^+) we use a moderately
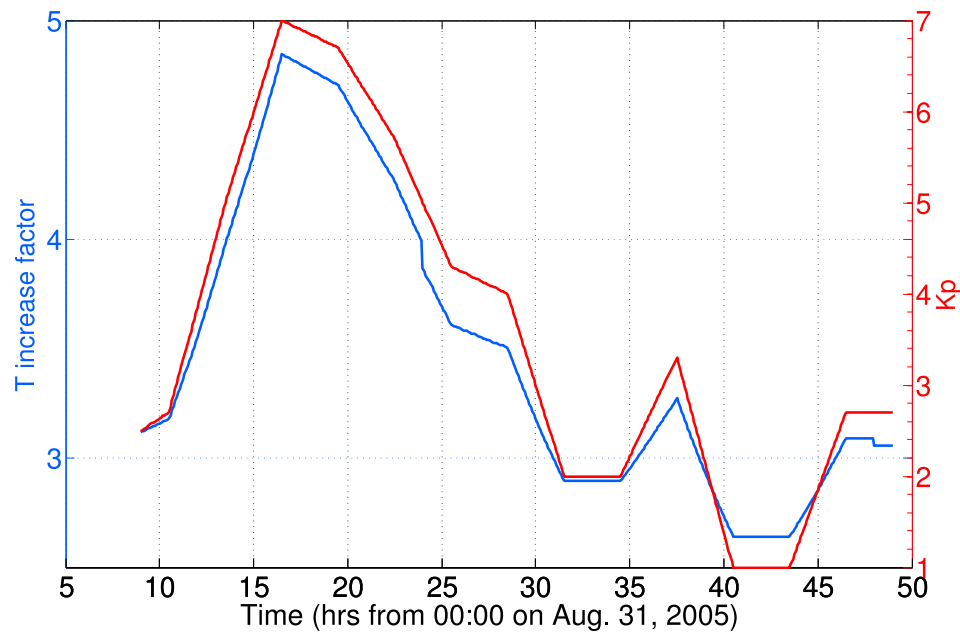
Figure 6. Ratio between temperature considering all ions versus temperature with only H^+ as a function of time (blue, left y axis) and corresponding Kp index (red, right y axis).

quiet time state obtained from measurements by the HYDRA and MICS instruments on the Polar spacecraft.

[55] Figure 9 shows, at 5 representative times T_1 through T_5, the ring current pressures obtained by different models: BATS-R-US, BATS-R-US+RCM, and RAM-SCB driven by SWMF (BATS-R-US+RCM+RIM) (both results with H^+ only and with all ion species, H^+, O^+ and He^+, are shown). The RAM-SCB results display one third of the trace of the
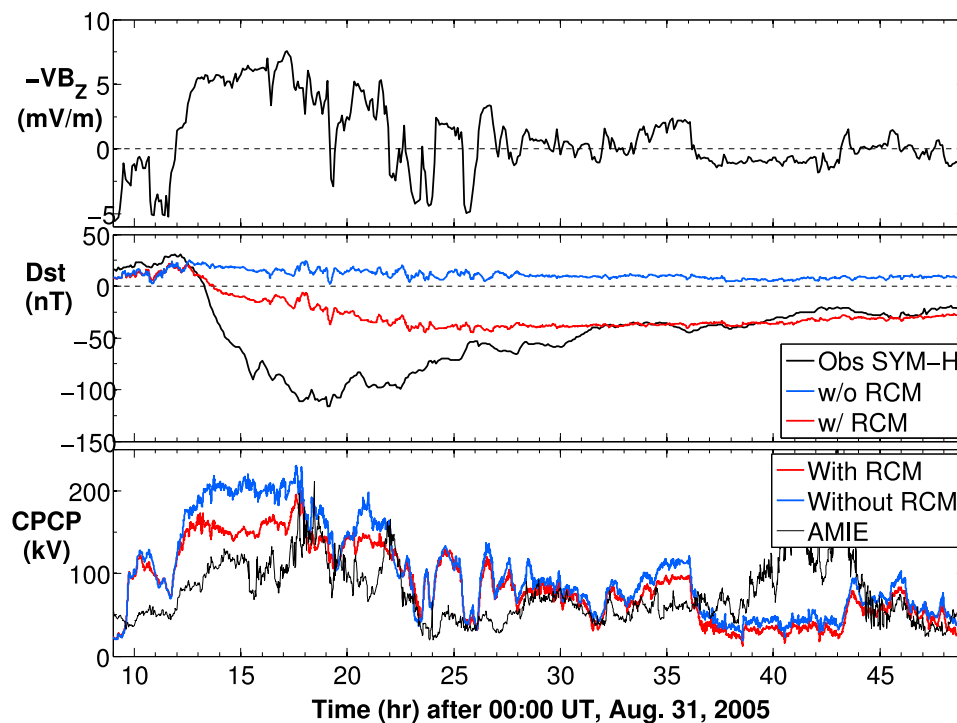

Figure 7. (top) Solar wind $-VB_z$ for the simulated event; (middle) Dst obtained from SWMF simulations (BATS-R-US+RIM in blue and BATS-R-US+RIM+RCM in red), as well as observed SYM-H (black); and (bottom) cross polar cap potential drop from SWMF runs (BATS-R-US+RIM (blue) and BATS-R-US+RIM+RCM (red)), as well as from AMIE (black).
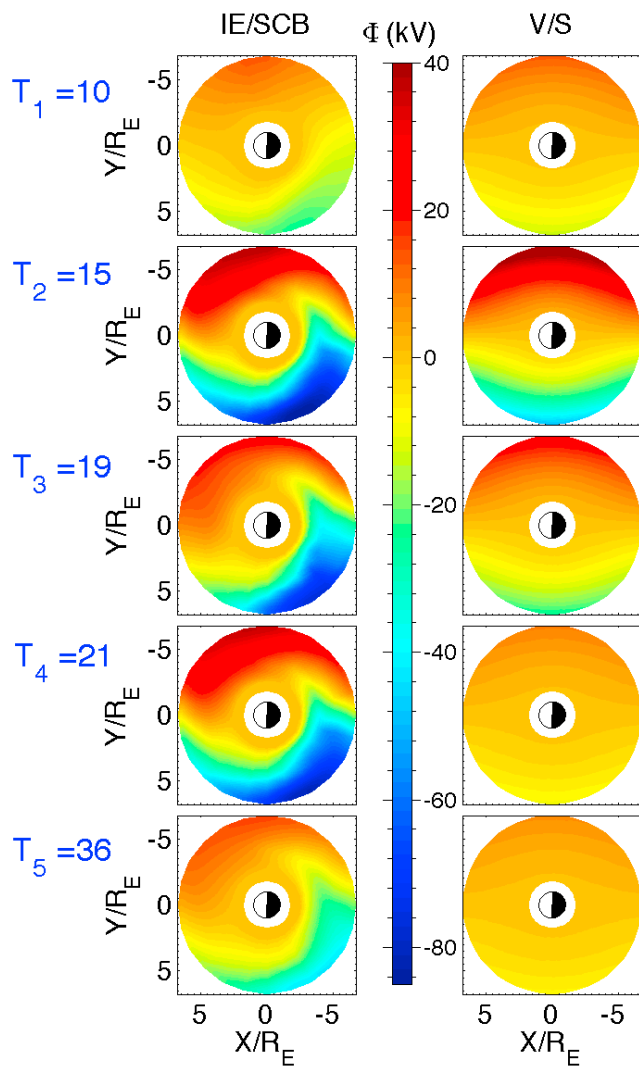
Figure 8. Electric potential in the equatorial plane for the simulated event: (left) RIM ionospheric values mapped along self-consistent magnetic field and (right) Volland-Stern empirical model values.

plasma pressure tensor, i.e., $(2P_\perp + P_\parallel)/3$ (the plasma anisotropy is presented in Figure 10). The plasma pressure increases significantly during the storm main phase, and peaks in the dusk sector for both SWMF with RCM and RAM-SCB simulations. The BATS-R-US run (alone) has very low plasma pressure throughout the event. The largest pressures within geosynchronous orbit domain are at hour 19, and are: 3 nPa for BATS-R-US, 38 nPa for BATS-R-US+RCM, 68 nPa for RAM-SCB (all ion species), and 313 nPa for RAM-SCB (H^+ only). The pressure peaks are in the pre-midnight local time sector for all models except BATS-R-US (its pressure peaks around midnight).

[56] The *Dst* index obtained with the different modeling approaches is shown in Figure 11. In the SWMF runs, *Dst* is obtained by Biot-Savart integration of the currents in the whole domain. In RAM-SCB, *Dst* is computed by using the Dessler-Parker-Sckopke (DPS) relation [*Dessler and Parker*, 1959; *Sckopke*, 1966]. Also shown in Figure 11 are the observed SYM-H, as well as SYM-H*, the value

after the contribution from the magnetopause currents is removed [*Burton et al.*, 1975; *O'Brien and McPherron*, 2000]:

$$\mathrm{SYM\text{-}H^*} = \mathrm{SYM\text{-}H} - b\sqrt{P_d(nPa)} + c \qquad (4)$$

[57] For *b* and *c* we use the values derived by *O'Brien and McPherron* [2000]: $b = 7.26$ and $c = 11$.

[58] The BATS-R-US simulation (alone) does not develop any significant (negative) *Dst*. The run with coupled RCM does develop *Dst*, with a minimum of −55 nT in 2 narrow spikes, at 1900 UT and 2300 UT (aside from those spikes, the *Dst* is around −45 nT near the storm peak). RAM-SCB with all ion species included develops a minimum *Dst* of −123 nT at ~1800 UT, the same time as the observed SYM-H minimum. With H^+ only, the minimum *Dst* is −235 nT, attained at about the same time. Both RAM-SCB simulations reproduce second minima in *Dst* at hour 22, also seen in observations. The RAM-SCB simulations start with a low (in absolute value) negative *Dst* value of −10 nT, a result of the initial condition. The best agreement with observations is the *Dst* value computed by the RAM-SCB with all species included. BATS-R-US+RCM significantly underestimates *Dst*, while RAM-SCB with only H^+ significantly overestimates it. BATS-R-US+RCM *Dst* has a very weak recovery to approximately −30 nT at hour 48. The RAM-SCB run with all ion species also has a much weaker recovery than seen in the observed SYM-H index; the RAM-SCB run with H^+ only significantly overestimates *Dst*, but has a stronger recovery.

[59] The pressure anisotropy $P_\perp/P_\parallel − 1$ is shown in Figure 10. It is significantly lower at the peak of the storm (19 h) compared to the recovery phase (36 h), a result also seen in observations [*Sorbo et al.*, 2005]. Large $P_\perp > P_\parallel$ anisotropy in the recovery phase appears at large L shells in the dusk-to-noon sector.

3.4. Field-Aligned Currents

[60] We calculate the field-aligned current (FAC) density in RAM-SCB by using a formula obtained from charge neutrality $\nabla \cdot \mathbf{J} = 0$. Considering separately $\mathbf{J}_\perp$ and $\mathbf{J}_\parallel$, the components perpendicular and parallel to the magnetic field $\mathbf{B}$, respectively, the charge neutrality relation becomes $\nabla \cdot (J_\parallel \mathbf{B}/B) = -\nabla \cdot \mathbf{J}_\perp$. With $\nabla \cdot \mathbf{B} = 0$, the left-hand side is equal to $\mathbf{B} \cdot \nabla(J_\parallel/B)$. Using the force balance equation $\mathbf{J} \times \mathbf{B} = \nabla \cdot \mathbf{P}$ to obtain $\mathbf{J}_\perp$, we finally obtain

$$\mathbf{B} \cdot \nabla \left(\frac{J_\parallel}{B}\right) = \frac{\nabla B^2 \times \mathbf{B} \cdot (\nabla \cdot \mathbf{P})}{B^4} = \frac{2\mathbf{B} \cdot (\nabla \cdot \mathbf{P} \times \kappa)}{B^2}. \qquad (5)$$

where $\kappa = (\mathbf{b} \cdot \nabla \mathbf{b})$ is the field line curvature. To obtain the field-aligned current density at a given location on a field line, we integrate equation (5) along the field line from the equatorial plane (where $J_\parallel = 0$) to that particular location.

[61] The obtained RAM-SCB field-aligned currents (Figure 12, third row) are mostly of region 2 sense, flowing into the ionosphere in the dusk sector and out of the ionosphere in the dawn sector.

[62] The RAM-SCB field aligned currents complement the BATS-R-US currents, which are of region 1 sense only and at higher latitudes (Figure 12, first row). The SWMF simulation with RCM included also leads to the appearance of region 2 currents as well (Figure 12, second row). They
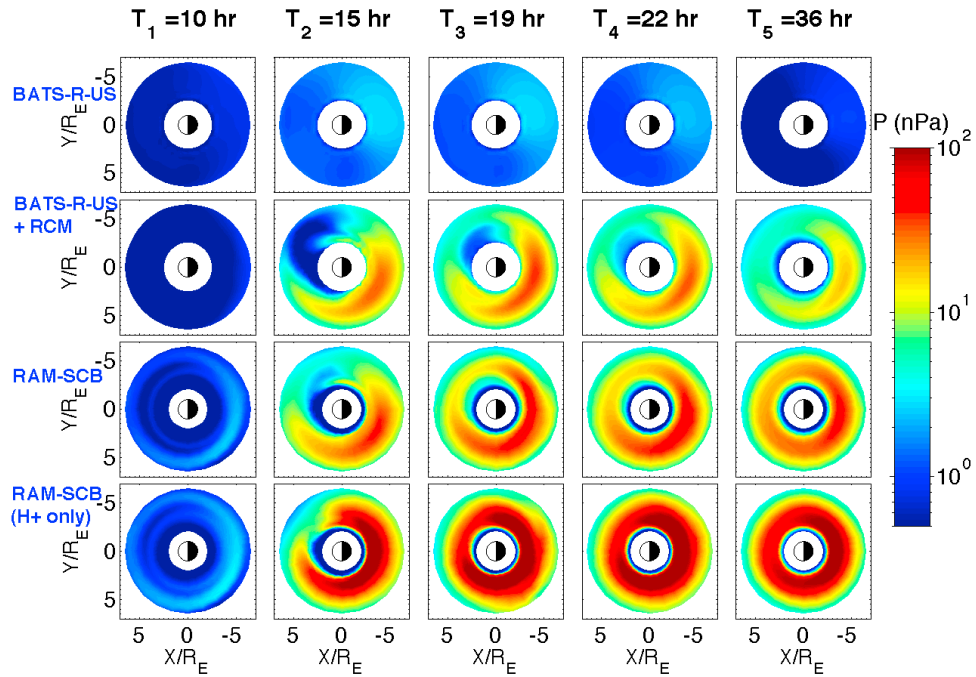
Figure 9. Equatorial plasma pressure from various simulations: BATS-R-US (first row), BATS-R-US+RCM (second row), RAM-SCB (all species) (third row), and RAM-SCB (H^+ only) (fourth row). RAM-SCB results show 1/3 of the trace of the pressure tensor. The RAM-SCB simulations are driven by SWMF (BATS-R-US+RCM) at the outer boundary. The BATS-R-US simulation domain only starts from $2.5 R_E$ from Earth.

are at similar locations and of slightly smaller magnitude than the RAM-SCB $J_\parallel$. The RAM-SCB currents are also more localized.

[63] For comparison, Figure 12 (fourth row) shows the current density inferred from Iridium measurements of the magnetic field vector deviation [*Anderson et al.*, 2002]. The maximum current density value is around $1 \mu A/m^2$, at the peak of the storm, which is similar to what RAM-SCB

(and SWMF with RCM) obtain at hour 19. Note that the Iridium $J_\parallel$ maps are averaged over 2 h, this time being needed to collect all the magnetic field observations for obtaining the global FAC pattern. Thus the Iridium current density features are understandably less sharp than the computed ones. The computed RAM-SCB currents reproduce some features of the Iridium ones especially in the recovery phase (1100 UT on 1 September): the region 2 current sheets
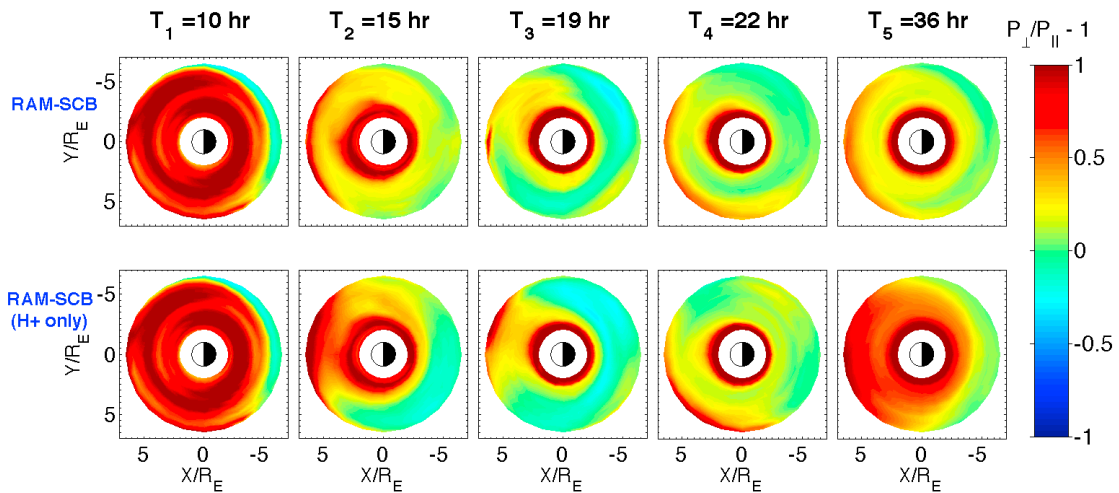

Figure 10. Degree of anisotropy $A = P_\perp/P_\parallel - 1$ from RAM-SCB runs: (top) all species included and (bottom) H^+ only.
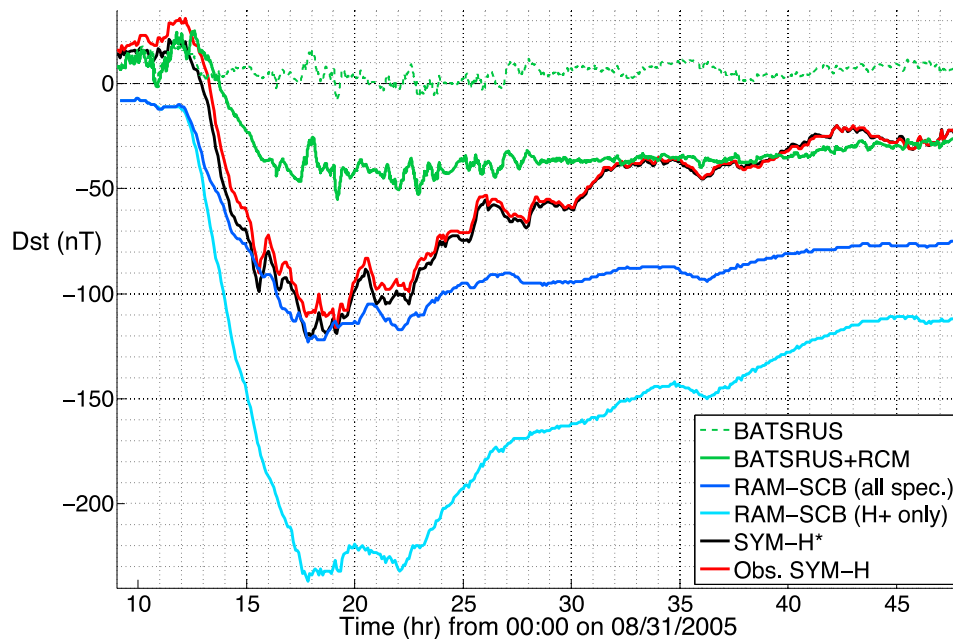
Figure 11. *Dst* index obtained from various runs: BATS-R-US (green dashed line), BATS-R-US+RCM (green solid line), RAM-SCB (all species) (blue solid line), and RAM-SCB (H^+ only) (cyan solid line). Also shown are the observed SYM-H (red line) and its magnetopause-corrected value SYM-H* (black line).

are clearly visible in both RAM-SCB output and Iridium observations (but very weak in the SWMF results).

3.5. In Situ Magnetic Field Comparisons With Satellite Data

[64] Several spacecraft with magnetic field data available during the 31 August to 2 September 2005 geomagnetic storm are Polar, Cluster and Geotail; their orbits are shown in Figure 13. The Geotail orbit is outside the RAM-SCB computational domain, so it will not be part of this analysis. In order to find the magnetic field at a satellite orbit, we find the nearest 4 neighbors in the RAM-SCB computational grid (which, while regular in Euler potential space, is an irregular point cloud in Cartesian space) and interpolate among them. To preserve accuracy, we consider the satellite outside the domain when the minimum distance between a grid point and the satellite location is larger than 0.15 R_E. Figure 14 shows data at Cluster 1, as well as magnetic field output by the model at the satellite location (for ease of comparison, we only plot the "external" field $\Delta\mathbf{B} = \mathbf{B} - \mathbf{B}_{dip}$). Cluster passes through the RAM-SCB computational domain only once during the simulated event, on the dayside during the recovery phase. Figure 14 shows that the model magnetic field reproduces the observed one reasonably well.

[65] Quantitatively, the RAM-SCB field is closer to observations than the dipole field (and the SWMF one), as evidenced by the lowest root mean square (RMS) error, defined as

$$RMS = \sqrt{\sum_{i=1}^{N}(\mathbf{B}_{mod} - \mathbf{B}_{obs})^2 / \sum_{i=1}^{N} B_{obs}^2}$$

The RAM-SCB magnetic field has $RMS = 0.05$, the dipole field $RMS = 0.13$ and the SWMF field $RMS = 0.32$. Comparing the computed field along the Polar spacecraft trajectory (for a time interval in the recovery phase in which the satellite orbit is within the RAM-SCB domain, as defined above) (Figure 15), we also find the RAM-SCB magnetic field most closely tracking the observed field at the spacecraft ($RMS_{RAMSCB} = 0.39$, $RMS_{dip} = 0.52$ and $RMS_{SWMF} = 0.47$).

4. Discussion

4.1. Plasma Sheet Conditions and Potential Electric Field in SWMF

[66] As shown in section 3.1, while the SWMF plasma output at 6.6 R_E may appear too cold and dense compared with in situ observations, this is based on the assumption that all ions are H^+. If other ions are considered in the plasma (especially O^+), the same MHD fluid will correspond to a more tenuous, hotter population that is much closer to observations.

[67] The cross polar cap potential drop (CPCP) (and by extension the electric potentials) are lower (and closer to observations) in the BATS-R-US+RCM simulation versus BATS-R-US alone, an effect previously reported by *De Zeeuw et al.* [2004] in BATS-R-US + RCM simulations. The effect of lowering CPCP was also found in the past when extra mass was introduced in global magnetosphere simulations [*Winglee et al.*, 2002; *Glocer et al.*, 2009b; *Brambles et al.*, 2010]. In those papers, one argument for the CPCP decreasing is the mass loading of the magnetosphere, leading to a decreased magnetic reconnection rate; another cause could be related to the region 2 field-aligned currents,
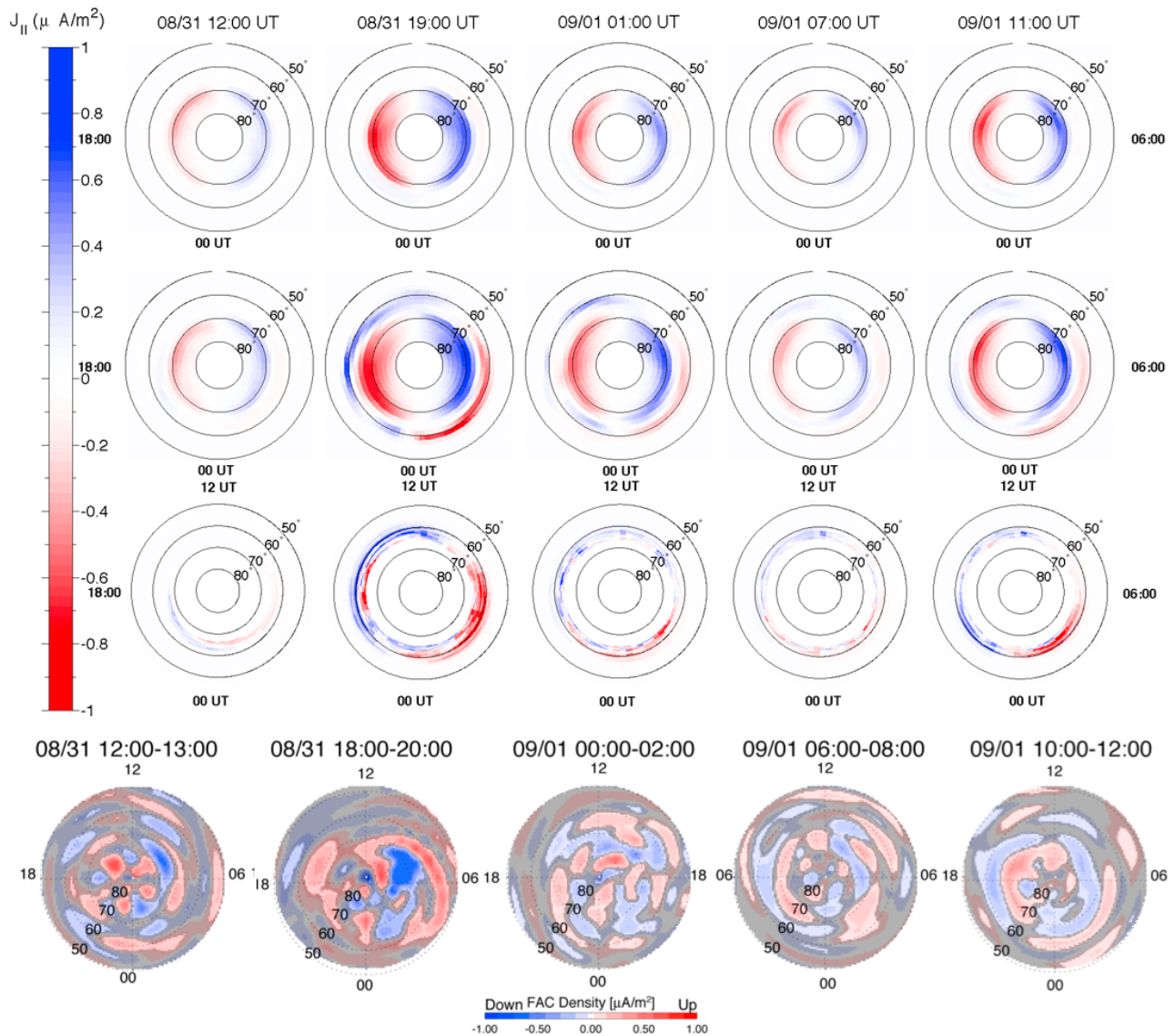
Figure 12. Field-aligned current density $J_{\parallel}$ in the ionosphere as obtained from the SWMF (BATS-R-US) (first row); same quantity but from the BATS-R-US+RCM run (second row); $J_{\parallel}$ from the RAM-SCB simulation (all ion species included) (third row); and $J_{\parallel}$ obtained from Iridium observations of magnetic field deviations, averaged over 2 h (1 h for the first plot) (fourth row).

as proposed by *Siscoe et al.* [2002]; finally, another explanation is the inflation of the magnetosphere/blunting of the magnetopause associated with a stronger ring current, leading to a wider magnetosheath and a magnetic flux diversion around the magnetosphere and less need for reconnection [*Brambles et al.*, 2010]. The inflation of the magnetosphere causes a 20% CPCP reduction in the study by *Brambles et al.* [2010], a percentage drop very close to what we find when adding RCM into SWMF. While no extra mass is introduced by the coupling with RCM, a much stronger ring current (and the corresponding inflation of the magnetosphere/blunting of the magnetopause) is one of the main effects of the coupling; based on the last theory above, this would lead to the observed reduction of the CPCP.

[68] The SWMF electric potentials are larger than the empirical Volland-Stern (V/S) ones, both in the main phase

of the storm and also in the recovery phase. In the main phase this fact is clearly due to the larger CPCP (the SWMF CPCP is larger than the AMIE values (Figure 7)). However, the SWMF CPCP is not larger than the AMIE one in the recovery phase, but the electric potentials in the RAM-SCB domain still exceed the V/S values. This could be caused by insufficient shielding by region 2 currents, even when BATS-R-US is coupled with RCM.

[69] Aside from the main phase increase in CPCP (from hours 12 to 17), of interest are 2 other spikes in the modeled CPCP, at ~hour 21 and hour 35. They very closely track increases in $-VB_z$ (Figure 7). In the AMIE CPCP, however, the first peak only appears at 2200 UT, while the second one does not appear at all. The peak at 2100 UT is also clearly seen in an increase in the electric potential (Figure 8)
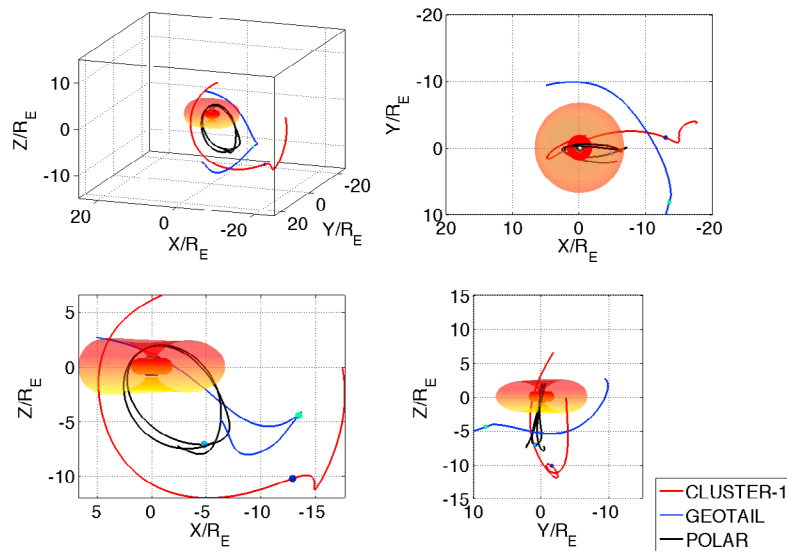
Figure 13. Orbits for the Polar (black), Cluster (red), and Geotail (blue) spacecraft during the September 2005 geomagnetic storm (SM coordinate system). The doughnut-shaped cavity of the RAM-SCB code is delimited by inner and outer Euler potential α surfaces.

compared to 1900 UT. No such increase is visible in the V/S potential, as Kp has no peak at that time. The 2 spikes in electric field at the times above lead to very clear signatures (with ~1 h delays) in the Dst profiles, as discussed in section 4.2.

4.2. Ring Current and *Dst*

[70] The BATS-R-US MHD code alone, as expected, does not develop a significant ring current (while the pressure increases somewhat in the inner magnetosphere, it is still an order of magnitude lower than inner magnetosphere kinetic models obtain; this order-of-magnitude difference is consistent with previous studies [e.g., *Toffoletto et al.*, 2004; *De Zeeuw et al.*, 2004; *Buzulukova et al.*, 2010]). Correspondingly, the Dst index from BATS-R-US is essentially zero (Figure 11). Coupling RCM into SWMF leads to a moderately strong ring current and a Dst index peak of −55 nT, about half of the observed value. The recovery of the ring current is not reproduced, however, most probably due to insufficient charge exchange losses.

[71] The RAM-SCB simulations lead to significantly stronger ring current and correspondingly Dst (the ring current energy and the Dst are interconnected through the DPS relation [*Dessler and Parker*, 1959; *Sckopke*, 1966]). In fact, the run with all ions assumed to be H^+ significantly overestimates the ring current and Dst (minimum computed Dst is −237 nT, compared with minimum observed SYM-H of −116 nT). The assumption of only protons being present in the MHD fluid is thus clearly inadequate. The run with all ion species (H^+, He^+ and O^+) taken into account leads to the best agreement with observations (minimum computed Dst of −123 nT). The overestimate with only H^+ is due to the fact that the SWMF plasma sheet is too cold and dense (also verified by a direct comparison with LANL data (Figure 5)); this cold plasma is not affected as much by gradient and curvature drifts as it is by the $\mathbf{E} \times \mathbf{B}$ drift, with the latter injecting it deeper into the inner magnetosphere (Figure 9),

leading to a very strong ring current. This preconditioning effect of a cold, dense plasma sheet on the ring current has been noted in both past simulations [e.g., *Lavraud and Jordanova*, 2007] and observational studies [*Lavraud et al.*, 2006]. While the electric field we use is obtained by RIM with shielding from the RCM region 2 currents, we note that a self-consistent shielding of the electric field by the actual, stronger RAM-SCB region 2 currents would likely mitigate this preconditioning effect and decrease the strength of the ring current, as shown by *Ebihara et al.* [2005].

[72] In contrast to the H^+ only simulation, the assumption of oxygen being present in the plasma sheet gives a much more tenuous (but hotter) particle population out of the MHD fluid code (in order to conserve the mass density and pressure) on the geosynchronous RAM-SCB boundary; this hotter population experiences faster gradient B and curvature drifts, and is not injected as deep into the inner magnetosphere.

[73] We note that a hotter particle population would also be obtained if our model boundary were extended past geosynchronous orbit (even considering H^+ the only ion species). It is likely that the cold MHD plasma would be energized by RAM-SCB from, e.g., 10 to 6.6 R_E to temperatures higher than the ones obtained from the MHD code at geosynchronous orbit. Results from simulations with an expanded RAM-SCB boundary will be reported in a future publication.

[74] Further comparing the proton versus all-ion simulations, we note that the ring current energy density (and contribution to Dst) is still predominantly from protons even in the simulation with other ion species (O^+, He^+) included. At storm peak (1800 UT on 31 August), the H^+ contribution to Dst is approximately −90 nT, the O^+ contribution is −28 nT, while the He^+ contribution is approximately −5 nT. These ratios are clearly dependent on the ion composition at the boundary, here taken from the *Young et al.* [1982] formula. Still, the above shows that the role
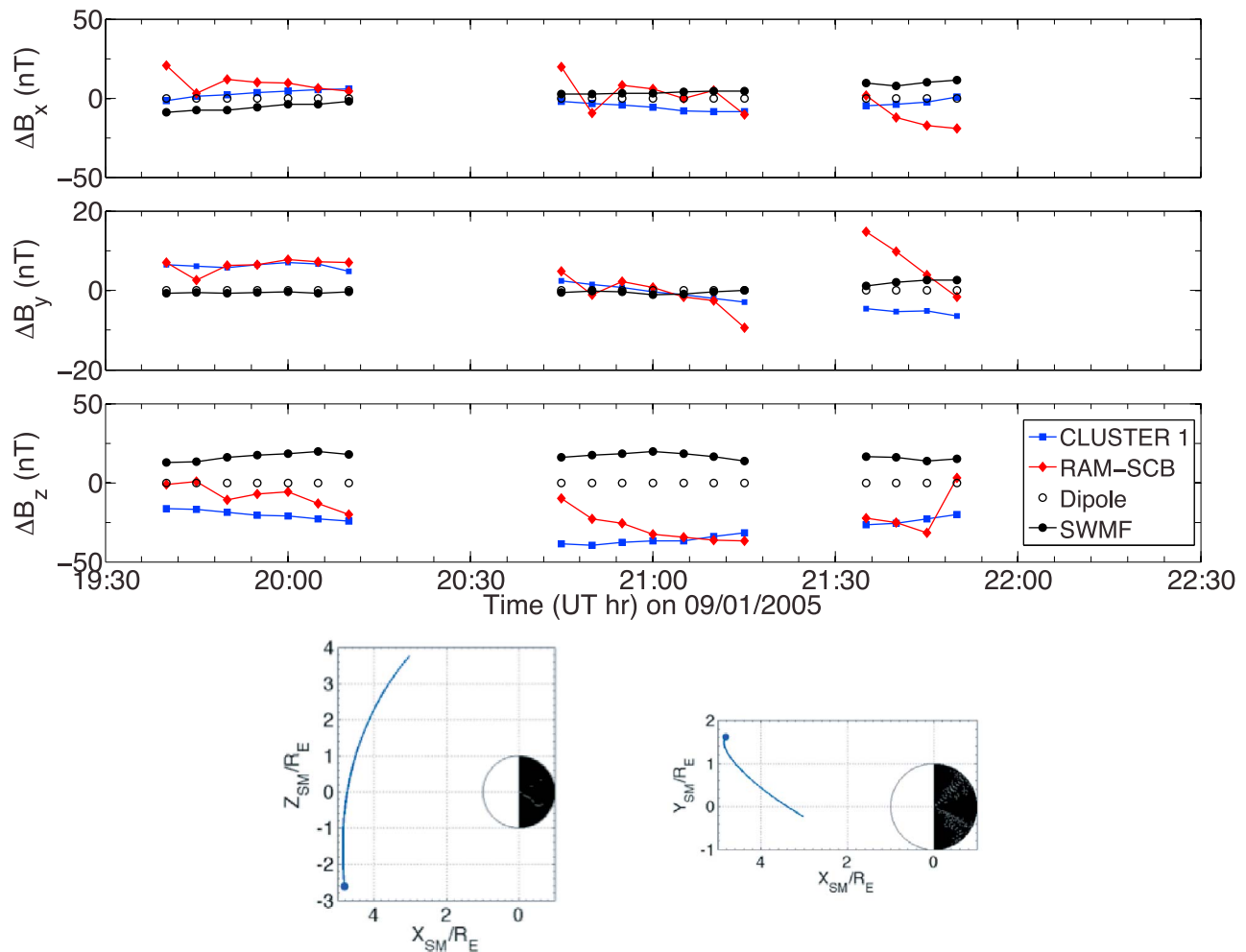
Figure 14. ΔB_X, ΔB_Y, and ΔB_Z as observed by Cluster 1 (blue), as well as computed by RAM-SCB (red) and SWMF (black). The dipole field is subtracted, so it corresponds to zero in the plots (shown as unconnected black circles). The gaps are where data are not available or when the spacecraft is outside the computational domain.

of much heavier (than H^+) O^+ in this simulation is mainly to lower the overall density of all particles (and increase their temperature) on the simulation boundary, leading to a lower overall ring current injection, in much better agreement with the observed *Dst*.

[75] The location of the ring current pressure peak is in the premidnight MLT sector in both BATS-R-US+RCM and RAM-SCB simulations. This location is consistent with that inferred from in situ observations of pressure and magnetic field deviations [e.g., *De Michelis et al.*, 1999; *Le et al.*, 2004]. While some studies [*C:son Brandt et al.*, 2002] have shown that ENA imaging during some events shows a postmidnight emission peak (in a limited energy range), a recent study using TWINS data (M.-C. Fok, GEM Workshop, private communication, 2009) has shown that such a postmidnight emission peak can still coexist with a premidnight overall pressure peak: the study showed through a data model (CRCM [*Fok et al.*, 1995]) comparison for an event on 11 October 2008 that while the peak in 12 keV H^+ flux tends to be in the post midnight sector, a careful inclu-

sion of all energy ranges still places the total plasma pressure peak in the premidnight local time sector.

[76] It is interesting to note that the 2 spikes noted in section 4.1 in the model CPCP (Figure 7) at hours 21 and 35 have clear equivalents in both computed *Dst* and observed SYM-H (Figure 11): at hour 22, 1 h after the increase in the electric potential, there is a second dip in *Dst* (observed in SYM-H, SYM-H*, and computed *Dst* for the RAM-SCB runs). Similarly, a smaller dip is seen at hour 36 in both observed and computed (RAM-SCB) *Dst*. This observational verification of increased ring current injections caused by spikes in CPCP is even more notable because the second spike is not visible in AMIE CPCP profile (even the first of the 2 spikes appears in the AMIE profile at hour 22, concomitant with the *Dst* drop, thus weakening the causality between the AMIE CPCP and the injection).

[77] Another interesting feature is the recovery of the ring current as seen in the *Dst* profiles. While the H^+ run has clearly too strong ring current, its recovery is much faster than the one in the simulation with all the ion spe-
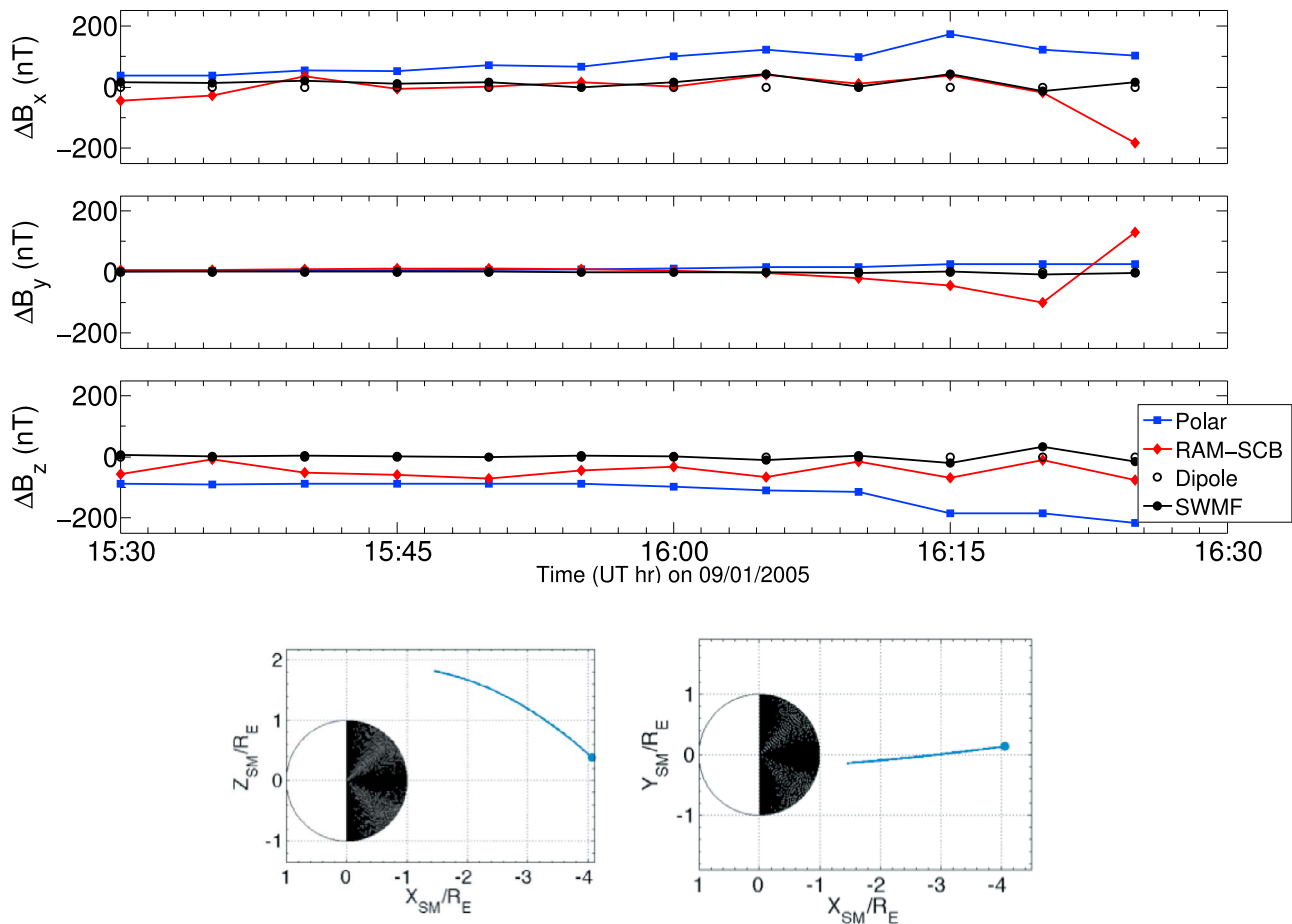
Figure 15. ΔB_X, ΔB_Y, and ΔB_Z as observed by POLAR (blue), as well as computed by RAM-SCB (red) and SWMF (black). The dipole field is subtracted, so it corresponds to zero (shown by unconnected black circles).

cies included. The latter's *Dst* does not recover as fast as observations show.

[78] The main ring current collisional decay mechanism is the process of charge exchange between the ring current ions and geocorona neutral atoms [e.g., *Daglis et al.*, 1999]. Charge exchange is modeled in RAM by assuming the geocoronal density model of *Rairden et al.* [1986]. Charge exchange losses are much higher in the H^+ only simulation, for the following cumulative reasons: (1) ions penetrate deeper in the inner magnetosphere, where the geocoronal density is higher, and (2) most importantly, the charge exchange cross section is much lower for the run with all ions, because that ring current plasma is significantly hotter.

[79] The H^+ simulation run, as discussed, has cold, dense plasma reaching deep into the inner magnetosphere. In the storm recovery phase, the partial ring current spreads out and forms a circular, more symmetric current quite close to Earth (Figure 9). That close to Earth geocoronal (exospheric) hydrogen density is large; the ring current is not too hot (temperature in the peak pressure region ~20 keV at 1900 UT), which makes for a large charge exchange cross section with geocoronal hydrogen; the ring current decays on a relatively fast time scale. On the other hand, the run with all ion species included has hotter, more tenuous plasma reaching not as close to Earth. The circular current in

the recovery phase is formed farther from Earth, where the geocoronal density is lower. At the same time, the ring current plasma contains significantly hotter particles than in the case with H^+ only (temperature in the pressure peak region ~50 keV at 1900 UT), because the particle distribution starts already with 3× to 5× higher temperature on the boundary; these hot ions have much lower charge exchange cross sections, leading to a weaker recovery of the computed *Dst* compared to the H^+ run. At the peak of the storm (1900 UT), in the H^+ only case the inner edge of the large pressure region is at ~2.5 R_E, while for the all ion run it is at ~3.5 R_E. Using the model by *Rairden et al.* [1986], the geocoronal H^+ density is about 2.7 times higher at 2.5 versus 3.5 R_E. At the same time, the cross section for charge exchange interaction with neutral hydrogen is about 5 times higher for a 20 keV proton compared to a 50 keV one. Both these effects cumulated lead to a much stronger ring current decay rate for the H^+ only ring current.

[80] The above discussion shows that the magnitude of the *Dst* peak is not the only constraint that an inner magnetosphere model should use for improving its inputs and physics processes. The recovery slope of the *Dst* also provides important information about the temperature and ion composition of the ring current plasma. A too slow recovery can indicate a too hot ring current. While we

applied the empirical relation of *Young et al.* [1982] to partition the MHD fluid into H^+, He^+ and O^+, more desirable in the future would be to use a multifluid model, where the different ion species are tracked separately and have different temperatures.

[81] We note that in the present study the RAM-SCB boundary is at geosynchronous orbit, and thus the *Dst* is computed from the energy density within the domain bounded at 6.5 R_E. Thus, the tail magnetotail current contribution, estimated by some to be up to 25% of the total *Dst* [*Turner and Baker*, 2000; *Ohtani et al.*, 2001; *Ganushkina et al.*, 2004], is not included in this study.

[82] Finally, we note that there is a dichotomy in the energization of low versus large pitch angle particles in the inner magnetosphere. This affects plasma anisotropy, a parameter important in wave excitation, thus making a fully anisotropic treatment like ours desirable. In the present RAM-SCB simulations, the lowest anisotropy in the storm main phase is on the nightside (Figure 10). The lowering of anisotropy there likely appears partly due to a more effective Fermi acceleration (increasing flux at low pitch angles and $P_\parallel$) compared to the betatron acceleration (increasing large pitch angle flux and $P_\perp$) in a decreased magnetic field, an effect studied before [*Zaharia et al.*, 2008]. Another cause for this particular day/night asymmetry in the pitch angle distribution is the drift shell splitting in the asymmetric field, which causes particle distributions on the nightside to be more field aligned, while the ones on the dayside more perpendicular, as first remarked by *Roederer* [1967].

4.3. Field-Aligned Current Behavior

[83] There is reasonable similarity (but not at all times) between the RAM-SCB region 2 (and SWMF region 1, as well as region 2 when RCM is included) results and the Iridium-inferred current density (Figure 12). At the beginning of the storm (1200 UT on 31 August), the RAM-SCB currents are very small. This corresponds in the Iridium observations to a complex, irregular pattern of low $J_\parallel$. The peak of the storm at 1800 UT corresponds to FACs of the same spatial pattern and magnitude in model and observations. The Iridium observations also see a much stronger region 2 FAC on the dawnside than duskside, a difference also present in the RAM-SCB model results. In the recovery phase, the magnitude of the modeled FACs tracks the observed one reasonably well. The best agreement between the modeled and observation-based currents is on 1 September 2005 at 1000 UT, when both model and observations show azimuthally broad field-aligned current systems. The fact that the best agreement is obtained in the later part of the recovery phase is not surprising, as it is then that the configuration does not change as much over an interval of 2 h (which is the time over which Iridium current patterns are averaged). The same 2 h average is likely responsible for the Iridium-derived patterns being broader than the RAM-SCB FACs at all times (the SWMF region 1 currents are broad as well, but this is likely due to the unavoidable numerical diffusion in the BATS-R-US grid).

[84] The region 2 currents that RAM-SCB produces in the main storm phase are consistent with the ring current pressure gradients, per the Vasyliunas relation (equation (5)). There are two main pairs of pressure gradients [e.g., *Buzulukova et al.*, 2010]: (1) radial from Earth (going out

from Earth, pressure first increases as one approaches the pressure peak region, then decreases) and (2) azimuthal (in local time). This first kind of pressure gradients is roughly parallel (or antiparallel) to the field line curvature and does not produce significant divergence of the perpendicular current (and thus no field-aligned currents). The largest contribution to the field aligned currents comes from azimuthal pressure gradients, directed eastward in the pre-midnight region and westward in the postmidnight region. These gradients lead to mostly region 2 currents in the inner magnetosphere, flowing into the ionosphere on the dusk-ward flank (where pressure increases with increasing MLT) and out of the ionosphere on the dawnside (where pressure decreases with increasing MLT). When the equatorial pressure peak rotates duskward (partial ring current region) during the storm main phase, this should lead to a corresponding rotation of the FAC pattern toward noon in the ionosphere. The peak location of the region 2 current is a complex function of the ring current morphology. The maximum region 2 FACs appear in the local time sector where the ring current changes fastest, as FACs result from ring current divergence. At the peak of the storm the computed partial ring current (PRC) is largest and rotated toward dusk. Thus, an azimuthal pressure gradient exists at the PRC edge on the dayside; the more the PRC rotates toward dusk, the more the location of this gradient rotates toward noon.

[85] The rotation of the computed region 2 current system toward noon in the storm main phase is clearly seen in the second column in Figure 12. In the Iridium-derived picture, there is a region 2 band extending to about ~1530 LT but no farther. The question is whether this rotation is realistic. The definitive answer to whether this rotation is clearly observed will have to wait until higher time resolution Ampere field-aligned current data is available. We note, however, that this effect was also obtained by the computations of *Liemohn et al.* [2001] (a FAC structure very similar to our results (in terms of rotation) is seen in Plate 1 of *Liemohn et al.* [2001]), and has also been inferred from ground-based observations [*Iyemori*, 1990].

[86] Finally, we note that here we compute the field-aligned currents in a fully magnetically self-consistent picture. Using Vasyliunas relation to calculate field-aligned currents without having computed a force balanced background state can lead to significant errors and spurious currents in regions where plasma $\beta_p > 1$, as shown by *Zaharia* [2008]. This is not an effect that can be neglected even in the inner magnetosphere, where β_p reaches 1 and higher during large storms such as the one analyzed here.

4.4. Magnetic Fields

[87] The RAM-SCB geosynchronous magnetic boundary is obtained by tracing the BATS-R-US magnetic field. That field is not very different from a dipole field at geosynchronous orbit (even for the BATS-R-US+RCM run). Our computational force balance method fixes the value of the Euler potential α on the outer boundary, with α computed from the BATS-R-US field. This constraint can limit the amount of stretching of the magnetic field in the interior of the domain, even with large plasma pressure inside (the solution of the force balance equation depends on both the pressure distribution and the magnetic boundary conditions). While the computed RAM-SCB magnetic field agrees rea-

sonably well with satellite observations (even on the dayside, the RAM-SCB magnetic field outperforms both a dipole and BATS-R-US), a drawback of the present geosynchronous boundary conditions is the inability to use the available GOES geostationary spacecraft magnetic field for comparison. For this, it is important that the RAM-SCB computational domain be extended away from geosynchronous orbit, an extension which is in progress.

5. Summary and Conclusions

[88] We report simulation results from a one-way coupling between RAM-SCB, a self-consistent inner magnetosphere model (the RAM code + a 3-D plasma equilibrium model with anisotropic pressure) and the Space Weather Modeling Framework (SWMF). RAM-SCB represents a significant improvement over our initial iterative self-consistent approach [*Zaharia et al.*, 2006, 2008; *Jordanova et al.*, 2006]: it employs full coupling every 5 min and has all the terms updated to use the force balanced magnetic field [*Jordanova et al.*, 2010]; also, it employs a new Euler potential technique in the equilibrium approach [*Zaharia*, 2008], allowing a seamless coupling of the equilibrium code with the fixed grid RAM model, without a need for extrapolation on the dayside [*Zaharia et al.*, 2006]. RAM-SCB is the first inner magnetosphere model in which the magnetic field is computed in three-dimensional force balance with fully anisotropic plasma pressures. Pressure anisotropy is a very important factor in inner magnetosphere physics, because it controls the excitation of plasma waves (whose interaction with particles can lead to acceleration and/or losses of both ring current plasma and radiation belts).

[89] Unlike in our previous studies where the model was driven by empirical inputs, in this work RAM-SCB is driven by another physics-based model, the SWMF. In this simulation setup, RAM-SCB obtains plasma and magnetic field boundaries at geosynchronous orbit from the BATS-R-US global magnetohydrodynamics (MHD) code within SWMF, and convection electric potentials in the ionosphere from the Ridley Ionosphere Model (RIM) within SWMF. The Rice Convection Model (RCM) is also included in the SWMF simulation to improve the plasma conditions for the RAM-SCB boundary and the convection electric field.

[90] Using this modeling setup we perform a comprehensive simulation of an actual event, the large storm of 31 August 2005 (SYM-H minimum of −116 nT). Comparing SWMF output at geosynchronous orbit with LANL satellite data we find the SWMF plasma too cold and dense if assumed to consist only of protons. This cold, dense plasma is injected by RAM-SCB very deep into the inner magnetosphere and leads to an unrealistically strong ring current. If heavier ions are considered (using an empirical model for the ion composition), the cold and dense plasma sheet problem is alleviated, and the resulting ring current and *Dst* profile during the main phase (including the peak value of the *Dst*) are in very good agreement with observations.

[91] We find that with BATS-R-US alone, the Cross Polar Cap Potential (CPCP) given by SWMF is too large compared with the observation-based AMIE model. With RCM included in SWMF, the CPCP decreases to more realistic values, possibly due to the ring current–caused inflation of

the magnetosphere and blunting of the magnetopause. With inputs from the optimal SWMF simulation run (RCM included in SWMF, heavy ion specification at geosynchronous orbit), we find that RAM-SCB reproduces well known features of the storm time inner magnetosphere, including ring current intensification and morphology, duskside local time peak location, pitch angle anisotropy, and total energy content. The RAM-SCB ring current and *Dst* index are 2× stronger than those computed by the SWMF and better reproduce observations, as seen by the very good agreement with the observed SYM-H peak and its time location. The ring current peak is in the premidnight local time sector, as verified by both particle and magnetic field in situ data. The ring current particle anisotropy $P_\perp/P_\parallel$ decreases on the nightside in the storm main phase, and increases during the recovery, with large values in the dayside magnetosphere, also agreeing with observations. The *Dst* index recovery provides important information about the temperature of the ring current (due to the strong dependence of the charge exchange cross section on temperature) and can constrain the model inputs in that regard. We also calculate field-aligned currents (mostly of region 2 sense) in the self-consistent RAM-SCB setting, and find they compare reasonably well with the 2 h averaged obtained from Iridium satellite data, especially during the storm recovery. As the ring current peak rotates duskward near storm peak, we find that the region 2 FACs rotate toward noon local time, a feature also seen both in other models and observations. Finally, a comparison of the RAM-SCB magnetic field output with in situ data from Cluster and Polar spacecraft finds that the RAM-SCB outperforms both the dipole and the SWMF field in reproducing observations.

[92] The present one-way coupling between the self-consistent RAM-SCB and the SWMF shows the importance of a kinetic self-consistent approach in properly describing inner magnetosphere physics and the sensitive dependence of the storm time magnetosphere on plasma sheet boundary, its ion composition and temperature, as well as the driving cross polar cap potential. The larger *Dst* compared with SWMF simulations with RCM coupled in suggests that completely replacing the inner magnetosphere with a self-consistent kinetic model in SWMF is preferable to just using the pressure from such a model in the global MHD code. This study also showcases the capability of RAM-SCB of providing a realistic physical description of the inner magnetosphere within a global MHD model. The RAM-SCB code is soon to be a full part of the Space Weather Modeling Framework, as an inner magnetosphere component. The full two-way coupling within SWMF needed for this is now in progress and will be presented in a future publication. In the two-way coupling, the large RAM-SCB pressure feedback will lead to stretching of the magnetic field lines in BATS-R-US and more realistic magnetic field boundaries. The region 2 field aligned current feedback is crucial in shielding the inner magnetosphere and will significantly modify the ionospheric electric potential patterns as well.

References

Anderson, B. J., K. Takahashi, T. Kamei, C. L. Waters, and B. A. Toth (2002), Birkeland current system key parameters derived from Iridium observations: Method and initial validation results, *J. Geophys. Res.*, *107*(A6), 1079, doi:10.1029/2001JA000080.

Belian, R. D., G. R. Gisler, T. Cayton, and R. Christensen (1992), High-Z energetic particles at geosynchronous orbit during the great solar proton event series of October 1989, *J. Geophys. Res.*, *97*(A11), 16,897.

Brambles, O. J., W. Lotko, P. A. Damiano, B. Zhang, M. Wiltberger, and J. Lyon (2010), Effects of causally driven cusp O+ outflow on the storm time magnetosphere-ionosphere system using a multifluid global simulation, *J. Geophys. Res.*, *115*, A00J04, doi:10.1029/2010JA015469.

Burton, R., R. McPherron, and C. Russell (1975), An empirical relationship between interplanetary conditions and *Dst*, *J. Geophys. Res.*, *80*(31), 4204.

Buzulukova, N., M.-C. Fok, A. Pulkkinen, M. Kuznetsova, T. E. Moore, A. Glocer, P. C. Brandt, G. Tóth, and L. Rastätter (2010), Dynamics of ring current and electric fields in the inner magnetosphere during disturbed periods: CRCM–BATS-R-US coupled model, *J. Geophys. Res.*, *115*, A05210, doi:10.1029/2009JA014621.

Cahill, L. J., Jr. (1966), Inflation of the inner magnetosphere during a magnetic storm, *J. Geophys. Res.*, *71*(19), 4505.

Cheng, C. Z. (1995), Three-dimensional magnetospheric equilibrium with isotropic pressure, *Geophys. Res. Lett.*, *22*, 2401.

Cheng, C. Z., and S. Zaharia (2004), MHD ballooning instability in the plasma sheet, *Geophys. Res. Lett.*, *31*, L06809, doi:10.1029/2003GL018823.

Courant, R., K. Friedrichs, and H. Lewy (1967), On the partial difference equations of mathematical physics, *IBM J. Res. Dev.*, *11*(2), 215, doi:10.1147/rd.112.0215.

C:son Brandt, P., S. Ohtani, D. G. Mitchell, M.-C. Fok, E. C. Roelof, and R. Demajistre (2002), Global ENA observations of the storm mainphase ring current: Implications for skewed electric fields in the inner magnetosphere, *Geophys. Res. Lett.*, *29*(20), 1954, doi:10.1029/2002GL015160.

Daglis, I. A., R. M. Thorne, W. Baumjohann, and S. Orsini (1999), The terrestrial ring current: Origin, formation, and decay, *Rev. Geophys.*, *37*(4), 407.

De Michelis, P., I. A. Daglis, and G. Consolini (1999), An average image of proton plasma pressure and of current systems in the equatorial plane derived from AMPTE/CCE-CHEM measurements, *J. Geophys. Res.*, *104*, 28,615.

Dessler, A. J., and E. N. Parker (1959), Hydromagnetic theory of magnetic storms, *J. Geophys.Res.*, *64*, 2239.

De Zeeuw, D., T. Gombosi, C. Groth, K. Powell, and Q. Stout (2000), An adaptive MHD method for global space weather simulations, *IEEE Trans. Plasma Sci.*, *28*(6), 1956, doi:10.1109/27.902224.

De Zeeuw, D. L., S. Sazykin, R. A. Wolf, T. I. Gombosi, A. J. Ridley, and G. Tóth (2004), Coupling of a global MHD code and an inner magnetospheric model: Initial results, *J. Geophys. Res.*, *109*, A12219, doi:10.1029/2003JA010366.

Ebihara, Y., M.-C. Fok, R. A. Wolf, M. F. Thomsen, and T. E. Moore (2005), Nonlinear impact of plasma sheet density on the storm-time ring current, *J. Geophys. Res.*, *110*, A02208, doi:10.1029/2004JA010435.

Fok, M.-C., T. E. Moore, J. U. Kozyra, G. C. Go, and D. C. Hamilton (1995), Three-dimensional ring current decay model, *J. Geophys. Res.*, *100*(A6), 9619.

Ganushkina, N. Y., T. I. Pulkkinen, M. V. Kubyshkina, H. J. Singer, and C. T. Russell (2002), Modeling the ring current magnetic field during storms, *J. Geophys. Res.*, *107*(A7), 1092, doi:10.1029/2001JA900101.

Ganushkina, N. Y., T. I. Pulkkinen, M. V. Kubyshkina, H. J. Singer, and C. T. Russell (2004), Long-term evolution of magnetospheric current systems during storms, *Ann. Geophys.*, *22*(4), 1317.

Glocer, A., G. Toth, M. Fok, T. Gombosi, and M. Liemohn (2009a), Integration of the radiation belt environment model into the space weather modeling framework, *J. Atmos. Sol. Terr. Phys.*, *71*(16), 1653, doi:10.1016/j.jastp.2009.01.003.

Glocer, A., G. Tóth, T. Gombosi, and D. Welling (2009b), Modeling ionospheric outflows and their impact on the magnetosphere, initial results, *J. Geophys. Res.*, *114*, A05216, doi:10.1029/2009JA014053.

Gloeckler, G., and D. C. Hamilton (1987), AMPTE ion composition results, *Phys. Scr.*, *T18*, 73.

Gombosi, T. I., D. L. DeZeeuw, C. P. T. Groth, K. G. Powell, and P. Song (1998), The length of the magnetotail for northward IMF: Results of 3D MHD simulations, in *Physics of Space Plasmas*, vol. 15, edited by T. Chang and J. R. Jasperse, p. 121, MIT Press, Cambridge, Mass.

Harel, M., R. A. Wolf, P. H. Reiff, W. Spiro, W. J. Burke, F. J. Rich, and M. Smiddy (1981), Quantitative simulation of a magnetospheric substorm: 1. Model logic and overview, *J. Geophys. Res.*, *86*, 2217.

Heinemann, M., and R. A. Wolf (2001), Relationships of models of the inner magnetosphere to the Rice Convection Model, *J. Geophys. Res.*, *106*(A8), 15,545.

Iyemori, T. (1990), Storm-time magnetospheric currents inferred from mid-latitude geomagnetic field variations, *J. Geomagn. Geoelectr.*, *42*, 1249.

Janhunen, P. (1996), GUMICS-3: A global ionosphere-magnetosphere coupling simulation with high ionospheric resolution, in *Proceedings of Environmental Modelling for Space-based Applications*, Eur. Space Agency Spec. Publ., *ESA-SP 392*, 205.

Jordanova, V. K., J. U. Kozyra, G. V. Khazanov, A. F. Nagy, C. E. Rasmussen, and M.-C. Fok (1994), A bounce-averaged kinetic model of the ring current ion population, *Geophys. Res. Lett.*, *21*(25), 2785.

Jordanova, V. K., L. M. Kistler, J. U. Kozyra, G. V. Khazanov, and A. F. Nagy (1996), Collisional losses of ring current ions, *J. Geophys. Res.*, *101*(A1), 111.

Jordanova, V., Y. Miyoshi, S. Zaharia, M. F. Thomsen, G. D. Reeves, D. Evans, C. Mouikis, and J. Fennell (2006), Kinetic simulations of ring current evolution during the Geospace Environment Modeling Challenge events, *J. Geophys. Res.*, *111*, A11S10, doi:10.1029/2006JA011644.

Jordanova, V., S. Zaharia, and D. Welling (2010), Comparative study of ring current development using empirical, dipolar, and self-consistent magnetic field simulations, *J. Geophys. Res.*, doi:10.1029/2010JA015671, in press.

Kubyshkina, M., V. Sergeev, N. Tsyganenko, V. Angelopoulos, A. Runov, H. Singer, K. H. Glassmeier, H. U. Auster, and W. Baumjohann (2009), Toward adapted time-dependent magnetospheric models: A simple approach based on tuning the standard model, *J. Geophys. Res.*, *114*, A00C21, doi:10.1029/2008JA013547.

Lavraud, B., and V. K. Jordanova (2007), Modeling the effects of cold-dense and hot-tenuous plasma sheet on proton ring current energy and peak location, *Geophys. Res. Lett.*, *34*, L02102, doi:10.1029/2006GL027566.

Lavraud, B., M. F. Thomsen, J. E. Borovsky, M. H. Denton, and T. I. Pulkkinen (2006), Magnetosphere preconditioning under northward IMF: Evidence from the study of coronal mass ejection and corotating interaction region geoeffectiveness, *J. Geophys. Res.*, *111*, A09208, doi:10.1029/2005JA011566.

Le, G., C. T. Russell, and K. Takahashi (2004), Morphology of the ring current derived from magnetic field observations, *Ann. Geophys.*, *22*, 1267.

Liemohn, M. W., J. U. Kozyra, C. R. Clauer, and A. J. Ridley (2001), Computational analysis of the near-earth magnetospheric current system during two-phase decay storms, *J. Geophys. Res.*, *106*(A12), 29,531.

Lyon, J. G., S. H. Brecht, J. D. Huba, J. A. Fedder, and P. J. Palmadesso (1981), Computer simulation of a geomagnetic substorm, *Phys. Rev. Lett.*, *46*(15), 1038, doi:10.1103/PhysRevLett.46.1038.

McComas, D. J., S. J. Bame, B. L. Barraclough, J. R. Donart, R. C. Elphic, J. T. Gosling, M. B. Moldwin, K. R. Moore, and M. F. Thomsen (1993), Magnetospheric plasma analyzer (MPA): Initial three-spacecraft observations from geosynchronous orbit, *J. Geophys. Res.*, *98*, 13,453.

Meng, X., G. Toth, and T. I. Gombosi (2009), BATSRUS with Hall MHD and anisotropic pressure, *Eos Trans. AGU*, *90*(52), Fall Meet. Suppl., Abstract SM51A-1344.

O'Brien, T. P., and R. L. McPherron (2000), An empirical phase space analysis of ring current dynamics: Solar wind control of injection and decay, *J. Geophys. Res.*, *105*(A4), 7707.

Ogino, T. (1986), A three-dimensional MHD simulation of the interaction of the solar wind with the Earth's magnetosphere: The generation of field aligned currents, *J. Geophys. Res.*, *91*, 6791.

Ohtani, S., M. Nosé, G. Rostoker, H. Singer, A. T. Y. Lui, and M. Nakamura (2001), Storm-substorm relationship: Contribution of the tail current to *Dst*, *J. Geophys. Res.*, *106*(A10), 21,199.

Olson, W. P., and K. A. Pfitzer (1974), Quantitative model of magnetospheric magnetic-field, *J. Geophys. Res.*, *79*, 3739.

Powell, K. G., P. L. Roe, T. J. Linde, T. I. Gombosi, and D. L. De Zeeuw (1999), A solution-adaptive upwind scheme for ideal magnetohydrodynamics, *J. Comput. Phys.*, *154*(2), 284, doi:10.1006/jcph.1999.6299.

Raeder, J., R. Walker, and M. Ashour-Abdalla (1995), The structure of the distant geomagnetic tail during long periods of northward IMF, *Geophys. Res. Lett.*, *22*, 349.

Rairden, R. L., L. A. Frank, and J. D. Craven (1986), Geocoronal imaging with Dynamics Explorer, *J. Geophys. Res.*, *91*(A12), 13,613.

Richmond, A. D., and Y. Kamide (1988), Mapping electrodynamic features of the high-latitude ionosphere from localized observations: Technique, *J. Geophys. Res.*, *93*(A6), 5741.

Ridley, A. J., D. L. De Zeeuw, T. I. Gombosi, and K. G. Powell (2001), Using steady state MHD results to predict the global state of the magnetosphere-ionosphere system, *J. Geophys. Res.*, *106*(A12), 30,067.

Ridley, A. J., T. I. Gombosi, and D. L. DeZeeuw (2004), Ionospheric control of the magnetosphere: Conductance, *Ann. Geophys.*, *22*, 567.

Roe, P. L. (1986), Characteristic-based schemes for the Euler equations, *Annu. Rev. Fluid Mech.*, *18*, 337.

Roederer, J. G. (1967), On the adiabatic motion of energetic particles in a model magnetosphere, *J. Geophys. Res.*, *72*, 981.

Sckopke, N. (1966), A general relation between the energy of trapped particles and the disturbance field near the Earth, *J. Geophys. Res.*, *71*, 3125.

Selesnick, R. S., and J. Blake (2000), On the source location of the radiation belt relativistic electrons, *J. Geophys. Res.*, *105*, 2607.

Siscoe, G. L., G. M. Erickson, B. U. Ö. Sonnerup, N. C. Maynard, J. A. Schoendorf, K. D. Siebert, D. R. Weimer, W. W. White, and G. R. Wilson (2002), Hill model of transpolar potential saturation: Comparisons with MHD simulations, *J. Geophys. Res.*, *107*(A6), 1075, doi:10.1029/2001JA000109.

Song, Y., S. Sazykin, and R. A. Wolf (2008), On the relationship between kinetic and fluid formalisms for convection in the inner magnetosphere, *J. Geophys. Res.*, *113*, A08216, doi:10.1029/2007JA012971.

Sorbo, M., F. Soraas, K. Aarsnes, K. Oksavik, and D. S. Evans (2005), Low latitude precipitation of energetic neutral atoms reflects the ring current pitch angle distribution during storms, *Eos Trans. AGU*, *86*(52), Fall Meet. Suppl., Abstract SM41C-1206.

Stern, D. (1975), The motion of a proton in the equatorial magnetosphere, *J. Geophys. Res.*, *80*(4), 595.

Toffoletto, F. R., S. Sazykin, R. Spiro, R. Wolf, and J. Lyon (2004), RCM meets LFM: Initial results of one-way coupling, *J. Atmos. Sol. Terr. Phys.*, *66*, 1361.

Tóth, G., et al. (2005), Space Weather Modeling Framework: A new tool for the space science community, *J. Geophys. Res.*, *110*, A12226, doi:10.1029/2005JA011126.

Tsyganenko, N. A. (1989), A magnetospheric field model with a warped tail current sheet, *Planet. Space Sci.*, *37*, 5.

Tsyganenko, N. A. (2010), On the reconstruction of magnetospheric plasma pressure distributions from empirical geomagnetic field models, *J. Geophys. Res.*, *115*, A07211, doi:10.1029/2009JA015012.

Tsyganenko, N. A., and D. P. Stern (1996), Modeling the global magnetic field of the large-scale Birkeland current systems, *J. Geophys. Res.*, *101*, 27,187.

Tsyganenko, N. A., H. J. Singer, and J. C. Kasper (2003), Storm-time distortion of the inner magnetosphere: How severe can it get?, *J. Geophys. Res.*, *108*(A5), 1209, doi:10.1029/2002JA009808.

Turner, N. E., and D. N. Baker (2000), Evaluation of the tail current contribution to *Dst*, *J. Geophys. Res.*, *105*(A3), 5431.

Van Leer, B. (1977), Towards the ultimate conservative difference scheme III. Upstream-centered finite-difference schemes for ideal compressible flow, *J. Comput. Phys.*, *23*, 263.

Volland, H. (1973), A semiempirical model of large-scale magnetospheric electric fields, *J. Geophys. Res.*, *78*(1), 171.

Wanliss, J. A., and K. M. Showalter (2006), High-resolution global storm index: *Dst* versus SYM-H, *J. Geophys. Res.*, *111*, A02202, doi:10.1029/2005JA011034.

Weimer, D. R. (1996), A flexible, IMF dependent model of high-latitude electric potentials having "space weather" applications, *Geophys. Res. Lett.*, *23*(18), 2549.

Weimer, D. R. (2001), An improved model of ionospheric electric potentials including substorm perturbations and application to the geospace environment modeling November 24, 1996, event, *J. Geophys. Res.*, *106*(A1), 407.

Winglee, R. M., D. Chua, M. Brittnacher, G. K. Parks, and G. Lu (2002), Global impact of ionospheric outflows on the dynamics of the magnetosphere and cross-polar cap potential, *J. Geophys. Res.*, *107*(A9), 1237, doi:10.1029/2001JA000214.

Wolf, R. A. (1983), The quasi-static (slow-flow) region of the magnetosphere, in *Solar-Terrestrial Physics: Principles and Theoretical Foundations: Based on the Proceedings of the Theory Institute Held at Boston College, August 9–26, 1982*, edited by R. L. Carovillano and J. M. Forbes, p. 303, D. Reidel, Dordrecht, Netherlands.

Young, D., H. Balsiger, and J. Geiss (1982), Correlations of magnetospheric ion composition with geomagnetic and solar activity, *J. Geophys. Res.*, *87*(A11), 9077.

Zaharia, S. (2008), Improved Euler potential method for three-dimensional magnetospheric equilibrium, *J. Geophys. Res.*, *113*, A08221, doi:10.1029/2008JA013325.

Zaharia, S., and C. Z. Cheng (2003), Can an isotropic plasma pressure distribution be in force balance with the T96 model field?, *J. Geophys. Res.*, *108*(A11), 1412, doi:10.1029/2002JA009501.

Zaharia, S., C. Z. Cheng, and K. Maezawa (2004), 3-D force-balanced magnetospheric configurations, *Ann. Geophys.*, *22*, 251.

Zaharia, S., V. K. Jordanova, M. F. Thomsen, and G. D. Reeves (2006), Self-consistent modeling of magnetic fields and plasmas in the inner magnetosphere: Application to a geomagnetic storm, *J. Geophys. Res.*, *111*, A11S14, doi:10.1029/2006JA011619.

Zaharia, S., V. K. Jordanova, M. F. Thomsen, and G. D. Reeves (2008), Self-consistent geomagnetic storm simulation: The role of the induced electric fields, *J. Atmos. Sol. Terr. Phys.*, *70*, 511, doi:10.1016/j.jastp.2007.08.067.

Zhang, Jichun, et al. (2007), Understanding storm-time ring current development through data-model comparisons of a moderate storm, *J. Geophys. Res.*, *112*, A04208, doi:10.1029/2006JA011846.

Zhang, Jie, et al. (2007), Solar and interplanetary sources of major geomagnetic storms ($Dst \leq -100$ nT) during 1996–2005, *J. Geophys. Res.*, *112*, A10102, doi:10.1029/2007JA012321.

V. K. Jordanova, D. Welling, and S. Zaharia, Space Science and Applications, Los Alamos National Laboratory, P.O. Box 1663, MS D466, Los Alamos, NM 87545, USA. (szaharia@lanl.gov)

G. Tóth, Center for Space Environment Modeling, University of Michigan, Ann Arbor, MI 48109, USA.